Interaction of relativistic H^- ions with thin foils

A. H. Mohagheghi, H. C. Bryant, P. G. Harris,* R. A. Reeder, H. Sharifian,† C. Y. Tang, and H. Tootoonchi‡
University of New Mexico, Albuquerque, New Mexico 87131

C. R. Quick and S. Cohen
Los Alamos National Laboratory, Los Alamos, New Mexico 87545

W. W. Smith
University of Connecticut, Storrs, Connecticut 06268

J. E. Stewart
Western Washington University, Bellingham, Washington 98225
(Received 10 August 1990)

The response of relativistic H^- ions to thin carbon foils was investigated for beam energies ranging from 226 to 800 MeV. For the foil thicknesses studied, ranging from 15 to 300 $\mu g/cm^2$, an appreciable fraction of the H^- beam survives intact, some H^- ions are stripped down to protons, and the remainder is distributed over the states of H^0. This experiment is different from the low-energy studies in that the projectile velocity is comparable to the speed of light, leading to an interaction time typically less than a femtosecond. The present results challenge the theoretical understanding of the interaction mechanisms. An electron spectrometer was used to selectively field ionize the Rydberg states $9 < n < 17$ at beam energies of 581 and 800 MeV. The yield of low-lying states was measured by Doppler tuning a Nd:YAG (where YAG represents yttrium aluminum garnet) laser to excite transitions to a Rydberg state that was then field ionized and detected. Data are presented for production of $n = 2,3$ at 226 MeV, $n = 2,3$ at 500 MeV, $n = 2,3,4$ at 581 MeV, $n = 2$ at 716 MeV, and $n = 1,2,3,4,5$ at 800 MeV. A simple model is developed to fit the yield of each state as a function of foil thickness. Although the simple model is successful in predicting the general features, the data are suggestive of a more complex structure, in the yield of a state as a function of the foil thickness. The optimum thickness to produce a given state increases with the principal quantum number of the state, suggesting an excitation process that is at least partially stepwise. The results of a Monte Carlo simulation are compared with the experimental data to estimate the distribution of the excited states coming out of a foil.

I. INTRODUCTION

What happens when a relativistic H^- ion goes through matter such as a carbon foil? For small carbon-foil thickness, 10^3–10^4 atoms thick, the H^- ion has a fair chance to emerge intact. This is surprising if we keep in mind that the H^- ion is larger than the spacing between the target atoms. Although total disintegration into two free electrons and a proton is another outcome, detachment of only one electron is quite probable for our range of thicknesses, with the residual hydrogen atom in an excited state. The interaction mechanisms that determine the charge fractions coming out of a foil and the resulting excited state distribution are not understood. Thus, the motivation of these experiments is to shed some light on the complex problem of relativistic beam-foil interaction mechanisms.

The beam-foil interaction has been primarily used to produce a variety of excited states of various atoms for spectroscopic studies.[1] However, recent work in atomic beam-foil spectroscopy has been directed toward the excitation processes. In a study of highly charged fast ions traversing a carbon foil, Yamazaki *et al.* found an enhancement of high-l states relative to a gas target.[2] Evidently, the basic mechanism for producing excited atoms in thin foils is different from that in gases, where the low-l states are favored. The enhancement of the high-l states is proposed to be the result of the stochastic motion of an electron in the field of the projectile leading to diffusion in angular-momentum states and energy.[3] This mechanism makes the existence of highly excited states of the projectile possible where according to previous views these excited states, with their large radii, could not exist because of screening and rapid collisional destruction.[4] A series of experiments, emphasizing the distribution of excited states, contribute to a better understanding of the interaction producing excited atoms in a foil.[5,6] A number of experimental and theoretical investigations[7–9] conclude that the distribution of excited states produced in a foil decreases as n^{-p}, where n is the principal quantum number and $p \approx 3$. The importance of the exit surface is demonstrated by a tilting-foil experi-

ment where the circular polarization of the radiation emitted by the excited atoms is shown to increase in magnitude as a function of the tilt angle.[10] Another study establishes the probability of electron capture by protons traversing to a foil to be a E_p^{-3} law, where E_p is the proton energy.[11] However, despite all the experimental and theoretical investigations, the nature of the beam-foil interaction, especially with relativistic beams, is still not well understood.

The experiment described here is one of the most recent in a series investigating the H^- ion using the relativistic H^- beam at the Clinton P. Anderson Meson Physics Facility (LAMPF) at the Los Alamos National Laboratory.[12–21] All the previous experiments have explored the behavior of the photodetachment cross section of the H^- ion in various electromagnetic fields. This experiment explores the response of relativistic H^- ions to a "matter field" (i.e., a thin foil), and differs in interesting ways from the low-energy experiments. The interaction time, during which the H^- ion experiences a perturbing force, is typically less than a femtosecond. The time of passage is comparable to the orbital time of the bound electrons so that the problem of transferring energy to the electrons might be quite complex. The initial wave function of the H^- ion can evolve into H^+, H^0, H^{0*}, with associated electron continua whose wave functions are reasonably well known, but the details of the interaction, which depend on the H^- velocity, foil thickness, and foil composition are not understood. This interaction, possibly a chaotic process, leads to a distribution of excited states depending on quantum numbers n, l, and m.

We have measured the yield of some excited states of hydrogen emerging from a foil using two experimental techniques. The first method detects Rydberg states by direct field ionization. The second method probes the low-lying states by exciting them to a Rydberg state with a Doppler-tuned laser. The laser-promoted states are then detected by field ionization. For the second method, our experimental energy resolution of about 1 meV is not sufficient to distinguish between the angular-momentum states of a given n manifold. Therefore, we have mainly focused our attention on measuring the yield for a given principal quantum number n as a function of foil thickness. One of the aims of this experimental study is to provide sufficient information on the production of the excited states to stimulate a theoretical study.

II. THEORY

A. Simple rate formula

A simple model, developed previously[22] to characterize charge-state distributions, has been extended to describe the yield of $H^{0*}s$ leaving a foil as a function of foil thickness. When the H^- beam penetrates a foil, there are three important processes that can take place assuming a series of interactions with individual target atoms:

(i) $H^- \rightarrow H^0(n)$, with cross section σ_{-n} ,

(ii) $H^0(n) \rightarrow \sum_{m \neq n} H^0(m)$, with cross section σ_{nm} ,

(iii) $H^- \rightarrow \sum_{m \neq n} H^0(m)$, with cross section σ_{-m} ,

where σ_{-n} is the one-electron detachment cross section of H^- leaving neutral atom in the state $H^0(n)$, σ_{nm} is the cross section for promoting $H^0(n)$ to a different excited state which includes the electron-loss process, and σ_{-m} is the total destruction cross section for H^- leading to an excited state other than $H^0(n)$, which also includes the two-electron-loss process. The process of electron capture from the target atoms on the surface of a foil is governed[11] by the E^{-3} law at the lower energies. By extrapolation, the cross section of target electron capture would therefore be much too small at energies of a few hundred MeV to play any role in formation of excited states. The differential equation expressing the yield of H^0s in state n is

$$\frac{dN_{H^0}(x)}{dx} = N_{H^-}(x)\sigma_{-n}\rho - N_{H^0}(x)\sigma_{nm}\rho \ , \tag{1}$$

where ρ is the target number density, and $N_{H^-}(x)$ and $N_{H^0}(x)$ are the numbers of H^- and $H^0(n)$ particles reaching a foil thickness x. Clearly,

$$N_{H^-}(x) = N_0 \exp[-(\sigma_{-n} + \sigma_{-m})\rho x] \ , \tag{2}$$

where N_0 is the initial number of H^- ions. The substitutions

$$y(x) = N_{H^0}(x), \quad a = \rho\sigma_{-n}, \quad b = \rho\sigma_{-m}, \quad c = \rho\sigma_{nm} \ , \tag{3}$$

lead to the following differential equation:

$$\frac{dy}{dx} = N_0 a e^{-(a+b)x} - cy \ . \tag{4}$$

Solving the differential equation with the condition that $y(x)$ is zero at $x = 0$, we get

$$y(x) = \frac{N_0 a}{a+b-c}(e^{-cx} - e^{-(a+b)x}) \ . \tag{5}$$

The thickness for maximum yield x_{max} follows from Eq. (5):

$$x_{max} = \frac{\ln[(a+b)/c]}{a+b-c} \ . \tag{6}$$

The solution to the simple model, Eq. (5), is used to provide a fit to the experimental yield data as a function of foil thickness.

B. Theoretical considerations

What does a relativistic H^- ion see as it penetrates a foil? A simple picture is that the ion encounters a periodic strong field produced by the target atoms which may be written as

$$F = A \sin(2\pi f t) \ , \tag{7}$$

with f given by

$$f = \frac{\gamma\beta c}{d} \ , \tag{8}$$

where γ and β are the usual relativistic parameters, c is

the speed of light, and d is the lattice spacing between the target atoms. As an example, consider the case of the H^- going through a carbon foil at 800 MeV. Then, we have $d=2$ Å, $\gamma=1.85$, and $\beta=0.84$, resulting in a frequency of 2.3×10^{18} Hz. If we think of this periodic electric field as a photon, then the equivalent photon energy is 9.5 keV which does not interact too effectively with the H^- ion. However, a more complete picture is that, for an amorphous target, the H^- ion encounters each target atom with a different impact parameter ρ. Then the observed ionization probability can be written as[23]

$$\langle P\rangle=\int_0^\infty w(\rho)p(\rho)d\rho\ , \tag{9}$$

where $p(\rho)$ is the individual ionization probability, and $w(\rho)$ is the weighting function used to average over the individual probabilities. Furthermore, the field encountered by the ion is not simply a single periodic function, but is a superposition of many different periodic fields. This raises the possibility of the existence of certain frequencies that could directly excite and ionize H^- ions and H^0 atoms.

One approach is to think of a foil interacting with the H^- beam as a square pulse of "matter field." One takes the point of view that the ionization and excitation processes may be to some extent coherent effects of all the interactions the ion encounters in its passage through the foil. As an example, Fig. 1(a) shows the "matter pulse" that an 800 MeV H^- might encounter when it is directed through a 40-μg/cm^2 carbon foil. The pulse is Fourier transformed from the time domain to the frequency domain, which gives the matter field strength as a function of frequency. We assume the response of the ion depends on the frequency of the pulse. We have therefore, for heuristic purposes, converted frequencies into energy E by multiplying by h. The square of this pulse gives the relative intensity spectrum of the matter field in the energy domain, which is

$$I_x(E)=\frac{F^2h^2}{\pi^2E^2}\sin^2\left[\frac{\pi TE}{h}\right]\ , \tag{10}$$

where

$$T=\frac{x\times10^{-8}}{\rho\gamma\beta c}\ . \tag{11}$$

Here F is the strength of the pulse, x is the foil thickness in μg/cm^2, ρ is the foil density in g/cm^3, γ and β are the usual relativistic parameters, and c is the speed of light in m/s [see Fig. 1(b)]. As the thickness of a foil is changed the positions of minima and maxima in the spectrum are moved. Thus, if we assume that the yield of a given state is proportional to the "matter field" intensity, then the yield of the state is modulated as we vary the foil thickness.

To get a glimpse of the hostility of the foil environment, consider the lifetime of an H^- ion in an electric field F as given by semiempirical equation,[24]

$$\tau=\frac{A_1}{F}\exp\left[\frac{A_2}{F}\right]\ , \tag{12}$$

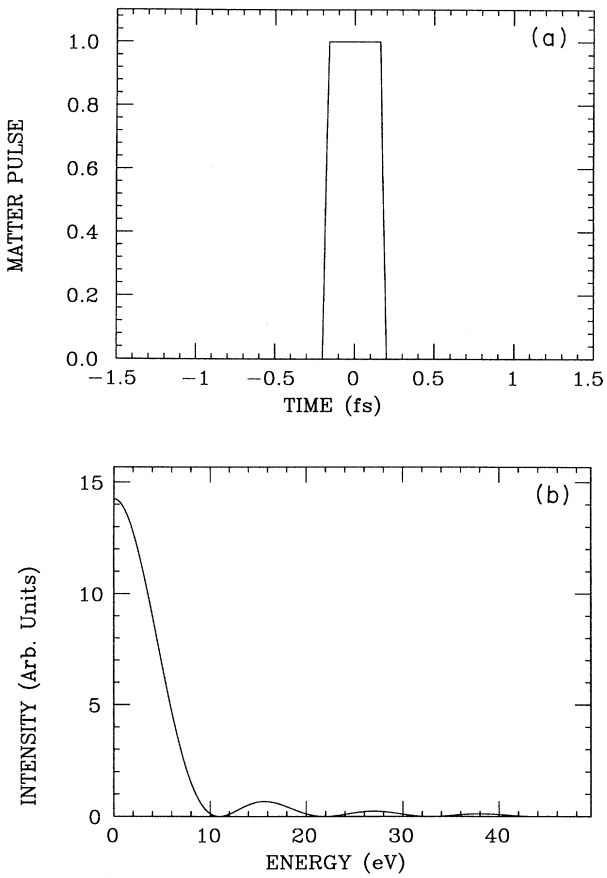

FIG. 1. (a) The "matter pulse" for a 40-μg/cm^2 carbon foil at 800 MeV; (b) the square of the Fourier transform of the "matter pulse" in 1(a).

where

$$A_1=2.47\times10^{-6}\frac{Vs}{m}\ , \tag{13}$$

and

$$A_2=4.494\times10^{9}\frac{V}{m}\ .$$

The Thomas-Fermi model of the carbon atom predicts a field of $\sim10^{12}$ V/m at a radius at a radius of one bohr radius (a_0), which inserted into Eq. (12) gives a lifetime of 2.5×10^{-18} s for the H^- ion, considerably less than the typical interaction time of 1 fs. The immediate question is, how is it possible for H^- ions to go through a foil intact as observed in the experiments? Further, the critical field for ionizing a hydrogen atom in some state n is given by[25]

$$F_c=\frac{5.713\times10^{-10}}{n^4}\text{V/m}\ . \tag{14}$$

We notice that the fields produced by the carbon atoms are much higher than the critical field needed to ionize even the $n=1$ state. Again, how is it possible that any

hydrogen atom is able to make it through a foil?

A possible solution to this dilemma may be to consider the beam-foil interaction a chaotic one. In an experiment by Galvez *et al.*,[26] a microwave field was used to ionize highly excited states of hydrogen atoms. It was observed that increased fields were needed to ionize the excited atoms whenever a parameter called the scaled frequency $n^3\omega$ became greater than 2. In this region, the driving frequency is greater than the classical orbital frequency. It was hypothesized that the increase in the field needed to ionize the Rydberg atoms is an indication of quantum chaos. Taking the frequency which the H^- encounters the target carbon atoms to be 800 MeV, we get a scaled frequency of 350 for $n=1$. This makes the beam-foil interaction an excellent candidate for quantum chaos. One of the consequences of chaotic behavior is that increased fields are needed to ionize atoms, possibly explaining why H^- ions and H^0 atoms are able to get through a foil intact.

An alternative picture is to think of a foil as a broadband intense high-frequency laser field which is turned on abruptly, with a pulse length of less than 1 fs. It has been shown by Su *et al.*[27] and Font[28] that atoms interacting with a high-frequency laser pulse tend to become saturated against ionization as the pulse intensity is increased. The stability is determined by the displacement amplitude of the free-electron response α_0, given by

$$\alpha_0 = -e\epsilon/m\omega^2 , \tag{15}$$

where ϵ is the electric-field amplitude, m is the mass of the electron, and ω is the angular frequency of the oscillation. If we take the frequency at which the H^- encounters the carbon atoms and an amplitude of 10^{12} V/m, then α_0 is 4.0×10^{-7} in atomic units, with the implication that electrons move very little during their passage through a foil. An extension of the numerical method of Su *et al.* to the case the "foil field" may provide important clues to the nature of the relativistic H^- beam-foil interaction.

Finally, a theory based on classical stochastic dynamics[3] may provide some insight into the nature of relativistic H^--foil interactions. This model used a microscopic Langevin equation of motion,

$$\frac{d\mathbf{v}}{dt} = -\nabla V_p + \mathbf{F}(t) , \tag{16}$$

to describe the motion of an electron during its passage through a foil. Here V_p is the screened potential of a highly charged ion, and $\mathbf{F}(t)$ represents the random forces that the electron experiences. The fluctuating force $\mathbf{F}(t)$ is described by a sequence of sudden, impulsive momentum transfers ("kicks"),

$$\mathbf{F}(t) = \sum_{\alpha=1,2} \sum_i \Delta\mathbf{P}_i^\alpha \delta(t - t_i^\alpha) , \tag{17}$$

where $\Delta\mathbf{P}_i^\alpha$ represents the stochastic momentum transfer to the electron per collision at time t_i^α, which is a random sequence. The parameter α is used to distinguish between scattering by the ionnic cores of the target atoms and scattering by the target electrons. The application of classical dynamics to Rydberg states is justified by their large quantum numbers (n,l). Thus, the approximation of an impulsive momentum transfer is valid for fast projectile electrons, where the collision time $t_c=\lambda_s/v_p$ is short as compared to the orbital period $T_n=2\pi n^3$ for a hydrogenic atom. λ_s is the static screening length of the medium. The stochastic motion of the electron leads to diffusion in angular momentum and energy, resulting in a large population of high-angular-momentum states. As the projectile exits the foil, the screened potential suddenly changes into a bare Coulomb potential, which closely resembles shakedown and shakeup processes in photoionization. The phase-space coordinates of the evolved electron at the time of passage through the surface $[\mathbf{r}(t_s),\mathbf{v}(t_s)]$ are used to construct orbits in the bare Coulomb potential, giving the final state of the projectile as it leaves the foil. This theory is successful in explaining the experimental data[2] taken with fast C^+ ions going through a carbon foil. It is interesting to note that if we take $\lambda_s=2.0$ Å, then the interaction time t_c for a hydrogen atom at 800 MeV is 4.3×10^{-19} s, which is short even when compared to the orbital time of the hydrogen atom in its ground state (1.52×10^{-16} s). This implies that the classical treatment of the beam-foil problem may remain valid even for small quantum numbers (n,l) for relativistic projectile velocities. A comprehensive application of the classical stochastic dynamics to the case of the relativistic H^- ions traversing a carbon foil may reveal the nature of the interaction mechanisms.

III. EXPERIMENTAL METHOD

The overall experimental arrangement is schematically shown in Fig. 2. Since the experimental hall is closed off

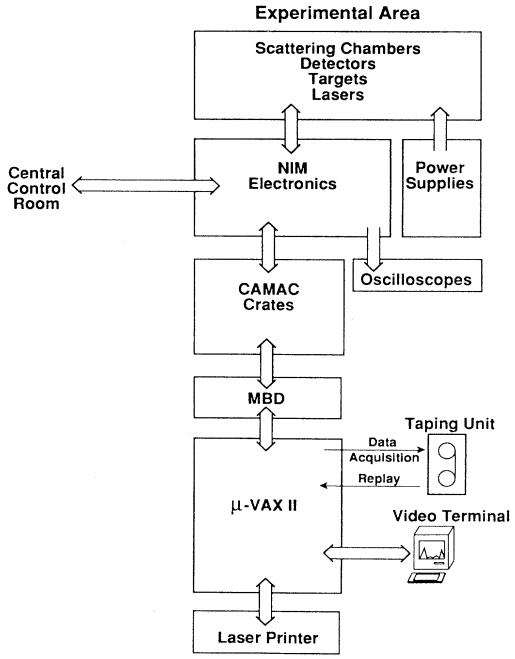

FIG. 2. Block diagram of the experimental arrangement at HIRAB.

when the beam is on to protect the personnel from the radiation exposure, all the equipment inside the experimental hall is controlled and monitored through a number of cables, each about 100 feet in length, from the high resolution atomic beam (HIRAB) counting house. All the incoming data signals are conditioned by the fast nuclear instrument module (NIM) electronics and sent to appropriate computer automated measurement and control (CAMAC) modules such as ADC's, TDC's, and scalers. The data contained in the CAMAC modules are read by a microprogrammable branch driver (MBD) at appropriate times and stored in the MBD memory buffer. Once the MBD buffer is full, the data are transferred to the μVAX-II memory, where the Q data-acquisition system puts the raw data on tape. The data are analyzed on line by a number of user-written codes producing histograms and data files. The computer is also used to send commands to various CAMAC modules that control equipment such as stepper motors and power supplies. A timing signal from the Los Alamos Meson Physics Facility (LAMPF) central control room is used to trigger the laser, open gates, and generate events for the computer to perform a number of predetermined actions. The following sections describe the experimental procedures in some detail—see Refs. 29 and 30 for a comprehensive discussion of the experimental techniques.

A. HIRAB beam line

The HIRAB is a facility dedicated to high-energy atomic physics. The facility is located at the end of the External Proton Beam (EPB) at LAMPF. The construction of HIRAB was completed by May 1987, with first test beam delivered by summer 1987. A major attraction of this facility is the all-year access to the building, allowing time for careful alignment work on lasers and optics. A moveable beam stop upstream of the experimental area permits personnel access to the area while other areas are receiving beam. A large concrete slab in the center of the building isolates delicate optical arrangements from unwanted vibrations. The beam line transport is capable of providing a low-divergence beam to the area. This is specially important for high-precision experiments performed at the Doppler-free angle, $\alpha=\cos^{-1}(-\beta)$, where the contribution of the beam momentum spread to the observed energy resolution vanishes to the first order. The divergence of the particle and laser beams in their common plane are the major parameters in determining the energy resolution of the experiment. The original design of the H^- beam optics uses two thin-foil strippers, producing a low-divergence beam, followed by a separated quadrupole magnet lens system, which achieves the final divergence by expanding the beam in one plane.[31] This design can provide a beam with a divergence as low as one μrad in one plane while maintaining a reasonable spot size. A compromise medium-resolution tune is currently used at HIRAB, resulting in a beam divergence of 10 μrad in the vertical plane. This tune is obtained without the use of the second slit collimator, allowing a higher beam intensity.

The experimental resolution can be further improved by reducing the momentum spread of the beam at 716 MeV by the momentum bunching technique developed in the summer of 1989.[32] Briefly, the lower energy is achieved by turning off the last five accelerating modules (modules 44–48). The last two modules, 47 and 48, are used to rebunch the beam. It was found that by adjusting the phase on module 48, the momentum spread was reduced by a factor of 5 from its initial value of 5×10^{-4}.

B. H^- and laser beams

The relativistic H^- beam is produced by the linear accelerator at the Los Alamos Meson Physics Facility (LAMPF). The primary beam at LAMPF runs at 120 macropulses a second. The H^- beam is delivered to HIRAB at repetition rates which usually range from 10 to 40 macropulses per second. The length of each macropulse is typically a few hundred μs. Each macropulse possesses a microstructure which is a series of micropulses of about 1-ns duration separated by 5 ns. Both the length of macropulse and the spacing between the micropulses can be adjusted to meet the experimental needs. We have received beam at HIRAB with macropulses ranging in duration from 500 ns to 800 μs, and micropulse spacing of 5 ns to 4 μs. A quantity of interest to the H^- experiments is the instantaneous beam intensity I(particles/micropulse), given by

$$I=6.24\times10^{6}\frac{\langle I\rangle S}{RM}\ , \tag{18}$$

where $\langle I\rangle$ is the average beam intensity in nA, S is the spacing between the micropulses in ns, R is the macropulse repetition rate in Hz, and M is the macropulse duration in μs. The average beam current required for the H^- experiments is typically of the order of a few tens of pA, which is a small fraction of the primary beam running at a few μA. It is evident from Eq. (18) that by adjusting the micropulse spacing and macropulse width we can vary the instantaneous intensity of orders of magnitude. Since the observed signal rate is directly proportional to I, then a high instantaneous current may be used to look at processes with a small cross section.

The Nd:YAG laser (Spectra DCR-2 Model) used for these experiments can be run in two modes. The first mode is a quasi-cw mode, where the laser pulse lasts for about 100 μs. The spot size is about 7 mm in diameter, and the beam divergence around 0.5 mr. A much shorter pulse is obtained by Q switching the laser through a Pockels cell. The resulting photon burst lasts about 8 ns with a nearly Gaussian temporal profile. This method provides an instantaneous laser power which is higher by orders of magnitude than the CW mode. The high intensity allows for efficient harmonic generation of up to the fourth multiple of the fundamental frequency of the Nd:YAG laser. Two ADP crystals with faces cut at the Brewster angle are angle tuned to generate the desired harmonics (532, 355, and 266 nm).

C. Laserless experiment

The highly excited states of hydrogen are detected by direct field ionization. Even though the details of the beam line are different from one run to another, all are conceptually shown in Fig. 3. A relativistic H^- beam is

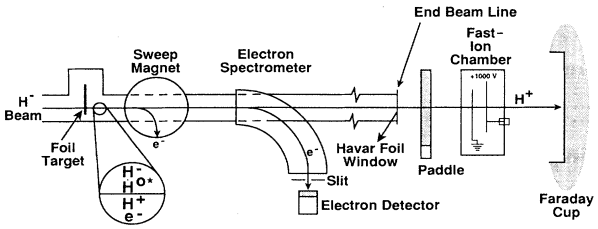

FIG. 3. Experimental setup for the laserless studies.

directed through a foil in one of the three different foil holders used in these experiments. A sweep magnet located downstream of the foil has a dual function. The first function is to bend the background electrons coming out of the foil out of the main beam. The second function is to selectively field ionize Rydberg states above a specified state. This helps to identify the peaks observed in the electron spectrometer downstream of the sweep magnet. The effect of the sweep magnet on a number of Rydberg states is demonstrated in Fig. 4.

The spectrometer is a sector magnet with entry and exit faces inclined at 22.5° to the design trajectory. The Rydberg atoms surviving the sweep magnet enter the electron spectrometer where the motional electric field seen by the atoms cause them to split into Stark states

$$H^0(n) \rightarrow \sum_{n_1,n_2,m} \mathrm{H}^0(n_1,n_2,m) , \tag{19}$$

where the (n_1,n_2,m) are the parabolic quantum numbers, with

$$n = n_1 + n_2 + |m| + 1 . \tag{20}$$

Each Stark state has a unique lifetime, which depends on the strength of the electric field. For a given set of substates associated with n, the Stark-shifted substate $(0,n-1,0)$ that lies lowest in energy has the shortest lifetime. The Stark-shifted substate $(n-1,0,0)$ that lies highest in energy has the longest lifetime. As a result, different Rydberg states decay at different positions within the spectrometer. The liberated electrons follow different trajectories, and the spectrometer field has to be adjusted in order to bring each state into the view of the detector. The electrons are then detected with a scintillator-photomultiplier combination. An example of electron trajectories for all the $n=11$ Stark states is shown in Fig. 5. A spectrum is formed by changing the spectrometer field and counting the number of electrons for each field as shown in Fig. 6. The first peak in Fig. 6 at 135.5 G is due to free electrons produced mainly from the surviving H^- ions colliding with residual gas molecules in the imperfect vacuum ($\approx 10^{-7}$ Torr) of the beam pipe. The second sharp peak at 141.0 G is the $n=11$ state, and the last broad peak at 147.0 G is the $n=10$ state. The sweep magnet is set at 70.0 G for this measurement, which field ionizes the $n=12$ state and above.

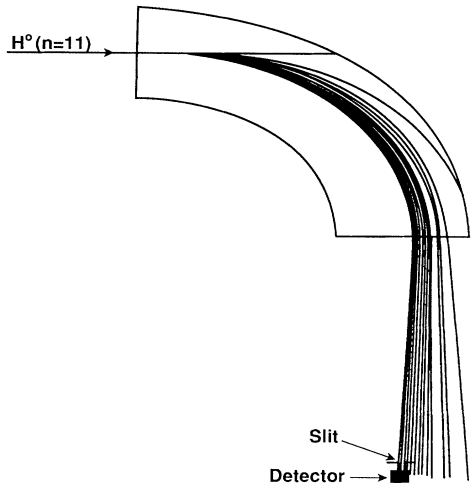

FIG. 5. Electron trajectories for the $n=11$ Stark substates at 800 MeV with the electron spectrometer set at 141.0 G.

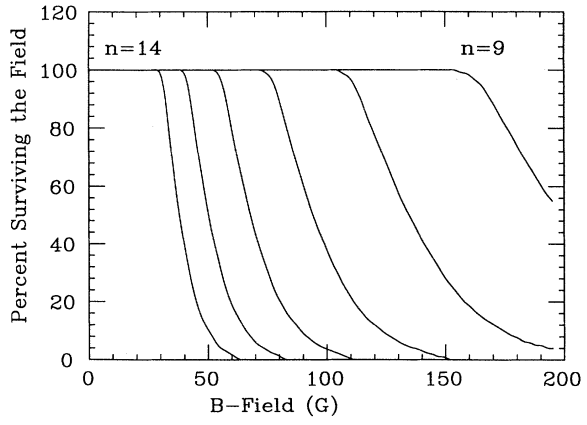

FIG. 4. Percent of Rydberg atoms surviving the field of the sweep magnet at 800 MeV. Each state is assumed to be equally distributed over its Stark substates.

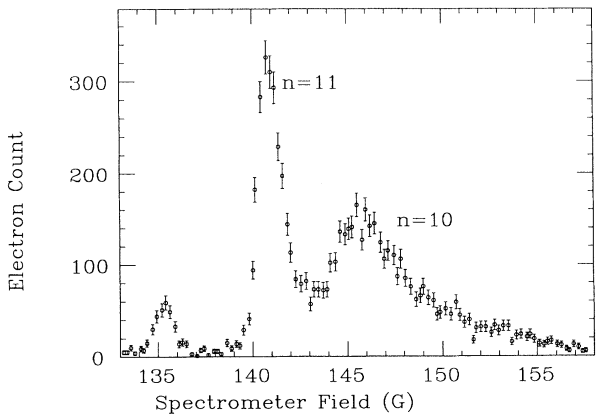

FIG. 6. Electron spectrum taken for a 19.0-μg/cm^2 carbon foil at 800 MeV.

A bending magnet downstream of the spectrometer guides all three beams through a "paddle" and a fast ion chamber. The paddle is a square piece of plastic scintillator mounted on a photomultiplier tube. The fast-response of the paddle, about 20 ns, allows us to monitor the individual micropulse intensities when they are separated by more than 20 ns. The fast-ion chamber with a response time of 10 μs probes the intensity of each macropulse. All the beams which are at this time stripped down to protons are stopped in a massive Faraday cup yielding the integrated beam current. The Faraday cup, 700 kg of graphite, is massive enough to completely stop the incident protons. The charge is drained off Faraday cup by a Teflon-insulated wire. The output current is digitized using a NIM current digitizer and is used to normalize the data to the beam current.

D. Laser experiment

The low-n states produced in a foil cannot be directly detected by field ionization. The required fields for ionization are too high for electron detection, as the radius of the curvature of the signal electron is too small. This prevents the electrons from reaching the electron detector. A fixed-frequency Nd:YAG laser, linearly polarized, is Doppler tuned in the rest frame of the atoms to excite a transition to a Rydberg state which is then detected by field ionization in the electron spectrometer. The conceptual experimental set-up is shown in Fig. 7. The H^- beam is incident on a foil in either of the three foil holders in the beam line. A bending magnet downstream of the foil has three functions. The first function is to sweep all the free electrons produced in the foil out of the beam line. The second function is to field ionize all the states with $n \geq 8$. The last function is to separate the H^-, H^0, and H^+ beams. The H^0 beam is intersected by the laser beam in the interaction chamber, where the intersection angle is changed with the aid of system of mirrors mounted on a turntable. The photon energy E in the atom's rest frame is given by

$$E=\gamma E_L(1+\beta\cos\alpha)\ , \tag{21}$$

where β and γ are the usual relativistic parameters, E_L is the photon energy in the laboratory frame, and α is the intersection angle defined such that $\alpha=0$ when the laser beam is head on to the H^0 beam. This method allows one to Doppler tune smoothly a fixed frequency laser over almost a decade of photon energies. A number of different lasers are used to obtain photon energies ranging from 0.045 up to 21.9 eV. The laser is Doppler-tuned to excite a transition from a low-lying state to a Rydberg state. Table I summarizes transitions investigated for these experiments and gives the harmonic of the Nd:YAG laser line (1.06μ) used.

TABLE I. Hydrogen transitions used for the laser studies at various beam energies (BE's). The harmonic of the Nd:YAG laser (1.06 μm) used is also shown.

BE (MeV)	Laser used	Initial n	Final n
800	4th YAG	1,2	11
800	1st YAG	2,3,4,5	11
716	4th YAG	1,2	12
581	1st YAG	2,3,4	13
500	1st YAG	3,4	13
226	2nd YAG	2,3	15

The signal rate is given by[33]

$$R=\frac{\sigma IJ(1+\beta\cos\alpha)}{G\beta\sin\alpha}\ , \tag{22}$$

where I and J are the instantaneous atomic and photon currents, respectively. The cross section σ can be calculated exactly from theory. A geometrical factor G represents the spatial and temporal overlap of the atomic and laser beams. Since we are unable to determine accurately the overlap, G becomes an arbitrary constant and we measure relative, not absolute, yields.

The electron spectrometer, located downstream of the interaction chamber, is tuned to detect the laser-excited Rydberg state with maximum efficiency. A spectrum is formed by plotting the number of electrons detected versus the photon energy, as shown in Fig. 8. The experimental energy resolution is not fine enough to resolve different angular-momentum states of a given state with principal quantum number n. Thus, all the angular-momentum states associated with a given state are smeared together, resulting in a near Gaussian spectral

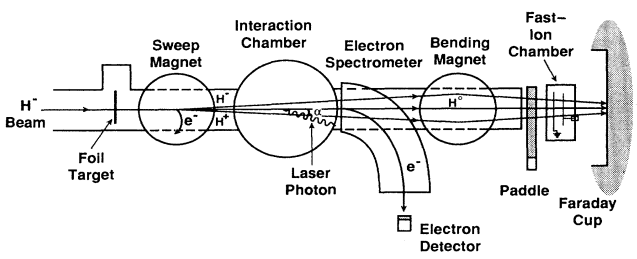

FIG. 7. Experimental setup for the laser studies.

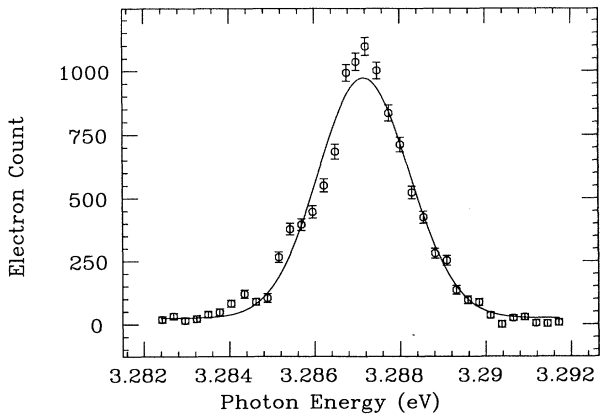

FIG. 8. $n=2-11$ transition taken at 800 MeV with the fundamental wavelength (1064.4 nm) of the YAG laser.

TABLE II. Summary of the laserless data and experimental conditions.

BE (MeV)	States detected	Macropulse length (μs)	Micropulse spacing (ns)	Date
581	12+ · · · +16	800	100	August '88
800	10,11	400	4000	July '89

line. In most cases the spectral line is fit to a Gaussian function and the area under the fitted curve is used as a measure of the yield of the state in question. In some cases, in order to speed up the data acquisition, the laser is kept fixed at an energy corresponding to the maximum amplitude as the yield from each of the foil samples is measured.

A second bending magnet, located downstream of the spectrometer, bends all the beams in the opposite direction of the first bending magnet. This is to prevent the spillage of the beams out of the beam pipe. All the beams then pass through the "paddle" and a fast-ion chamber monitoring the fluctuations in instantaneous beam current. Finally, all the beams, which are now are stripped down to protons, end up in a massive Faraday cup. The Faraday cup is again used to normalize the data taken at each intersection angle to the beam current. The normalization is set to get about 100 laser shots for each intersection angle.

IV. DATA AND ANALYSIS

In this section the details of data analysis are discussed. In particular, the procedures to obtain the relative yield of a given state for various modes of data acquisition are explained. The simple rate equation, Eq. (5), is used to fit the experimental data on the relative yield of a particular state as a function of the foil thickness. A program, MINUIT,[34] is employed to fit the simple rate equation by minimizing the χ^2 as given by

$$\chi^2=\sum_i \frac{[Y_i^t(x)-Y_i^e(x)]^2}{\sigma_i^2} , \tag{23}$$

where Y_i^t are the predictions of the simple rate equation, Y_i^e are the experimental points, and σ_i are the standard deviations associated with each data point. In our case the statistical errors are used for the fitting. The largest source of the systematic errors is the uncertainty in thickness of a given foil. Once a fit is completed, the errors caused by the foil-thickness uncertainties are added in quadrature to the statistical errors to obtain a modified value for the reduced χ^2.

A. Laserless data

The laserless experimental technique is used to investigate the Rydberg atoms at beam energies of 581 and 800 MeV. The details of the experiments and fits are discussed in the following sections. Table II summarizes the experimental conditions.

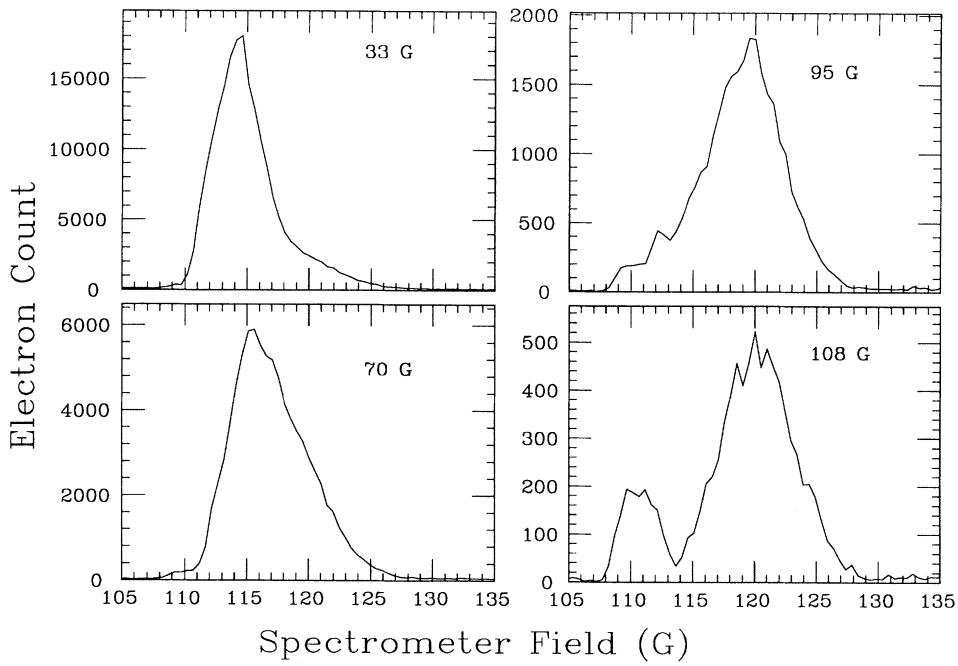

FIG. 9. Response of the electron spectrum to the magnetic field of the sweep magnet at 581 MeV for a 40.0-μg/cm^2 carbon foil.

1. *Yield of Rydberg states at 581 MeV*

This experiment was done with a 581-MeV polarized H^- beam which was delivered in macropulses of 800 μs in duration with a microstructure of pulses 0.25 ns wide every 100 ns. The yield of the Rydberg states were measured by the electron spectrometer. Unfortunately, a 1.5-mm-wide slit was missing during the experiment, leaving a 2.5-cm-long acceptance window along the beam direction. This smeared the Rydberg states together. Figure 9 demonstrates the response of the electron spectrum to various settings of the sweep magnet for a 45-$\mu g/cm^2$ carbon foil. The sweep magnet was then fixed at 32.5 G and the spectrum for each foil was measured. The total yield of all the detected Rydberg states, $n=11-16$, for each foil was simply determined by summing all the bins in a given spectrum. The data for each point corresponds to a total charge of 5.0 nC (i.e., 3.12×10^{10} H^- ions) integrated by the Faraday cup. The result, illustrating how the total yield of Rydberg atoms is affected by the foil thickness, is shown in Fig. 10. The solid line is the best fit to the simple rate equation. The results of the fit are summarized in Table III. The calculation for reduced χ^2 takes into account the foil-thickness uncertainty. The number of the degrees of freedom f is determined by subtracting the number of fit parameters from the number of data points. The confidence level of the fit is 3.1×10^{-4}%. The statistical error bars are obtained, assuming Poisson statistics, simply by taking the square root of each data point. The deviation of the reduced χ^2 from the expected value of 1.0, for a good fit, is evidence that an extension of the simple rate equation is needed.

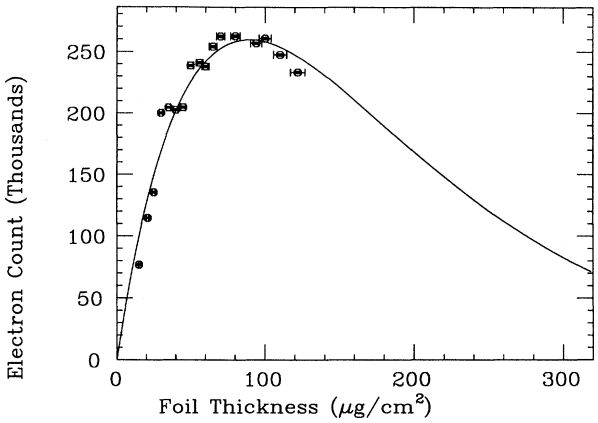

FIG. 10. Relative yield of Rydberg atoms at 581 MeV. The solid line is the best fit to Eq. (5).

2. *Yield of $n=10,11$ at 800 MeV*

The H^- beam was delivered to HIRAB at 10 Hz with macropulses lasting for 400 μs. The micropulses were spaced by 4 μs. This beam structure produced intense micropulses with about 6.0×10^6 H^- ions per micropulse at an average current of 1 nA. As a result, running at high currents produced multiple signal counts in each macropulse. This posed a problem, as the experiment was set up to simply count the signal electrons. We used a LeCroy qvt module to digitize the pulse height of the signal for a sample of micropulses since the dead time of the ADC, about 10 μs, did not allow digitizing the signal from each micropulse. The pulse-height spectrum verified the problem of multiple counts. The problem was resolved by employing the following two methods: First, the sweep magnet field was fixed at 70.0 G, which field ionized states with the principal quantum number greater than 11. Second, the beam current was turned down to about 2 pA. No multiple counts were observed after going through the above procedure.

A slit of 1.65-mm width was in place in the spectrometer which helped to resolve the $n=10$ and 11 peaks (see Fig. 6). The first small peak in Fig. 6 is due to electrons produced by the remaining H^- ions colliding with the residual gas molecules in the beam pipe. The sharp peak in

TABLE III. Results of fitting the relative yield of observed excited states to the simple rate equation. The reduced χ^2 for each fit takes into account the errors caused by the foil-thickness uncertainty. N_0 is a relative amplitude only.

n	BE (MeV)	N_0	$10^{-3}a$ ($cm^2/\mu g$)	$10^{-3}b$ ($cm^2/\mu g$)	$10^{-3}c$ ($cm^2/\mu g$)	χ^2/f	CL (%)
1	800	54700±600	38.8±1.1	9.49±0.55	10.9±0.2	0.61	83.57
2	800	226.7±2.7	41.9±0.2	2.1±0.6	12.6±0.2	2.93	0.04
3	800	66.5±0.2	12.3±0.3	0.9±0.8	13.1±0.2	3.01	0.03
4	800	32.3±0.4	5.52±0.09	5.89±0.24	11.4±0.2	1.92	2.74
5	800	9.24±0.08	5.2±0.1	6.2±0.3	11.3±0.3	2.01	1.96
10	800	12140±40	18.8±0.1	0.09±0.08	5.76±0.05	6.07	0.00
11	800	11380±50	13.06±0.09	0.74±0.09	9.28±0.07	4.94	0.00
2	716	1065±18	52.0±3.3	5.69±0.97	11.9±2.5	0.69	76.68
2	581	9270±120	29.1±0.8	7.32±0.59	20.8±0.4	2.99	0.02
3	581	2770±120	12.18±0.54	1.66±0.21	13.84±0.34	2.48	0.22
4	581	7990±90	7.979±0.120	5.08±0.29	13.06±0.29	4.28	0.00
14	581	806300±400	9.531±0.072	1.366±0.014	10.90±0.02	3.84	0.00
3	500	440±50	15.31±1.70	0.003±0.002	15.26±1.90	2.75	0.50
4	500	980±40	12.6±0.6	0.007±0.006	10.7±0.6	2.25	2.10
2	226	44500±600	76.0±3.0	36.0±1.0	23.0±3.0	2.49	0.29

the middle is the $n=11$ state and the following broad peak is the $n=10$ state. The hydrogen peaks are fit to three asymmetric Gaussians. The area under the first Gaussian peak is used to estimate the yield of $n=11$. The areas of the last two Gaussian peaks are used to estimate the yield of $n=10$ state. Figures 11(a) and 11(b) show the yields of $n=10$ and 11 as a function of foil thickness. The solid line in each graph is the best fit of the simple rate equation. The results of the fit are tabulated in Table III.

The first small peak in the spectrum, free electrons produced mainly from H^- ions colliding with the residual gas in the vacuum, is independently fit to a Gaussian function. This signal allows for a crude measurement of the fraction the H^- beam surviving the foil (see Fig. 12). There is a constant background, due to a halo associated with the primary H^- beam, which obscures the electron peak for the thicker foils. The signal is fit to the following function:

$$Y(x)=Ae^{-bx}+C\ , \tag{24}$$

taking into account the exponential attenuation of the

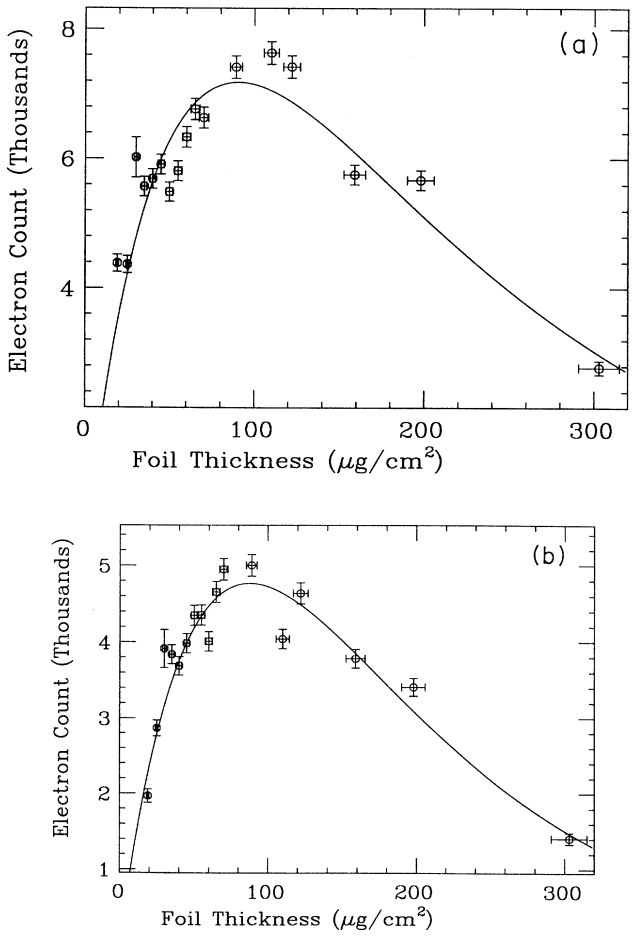

FIG. 11. Relative yield of (a) $n=10$ and (b) $n=11$ at 800 MeV as a function of carbon-foil thickness. The solid line in each graph is the best fit to (5).

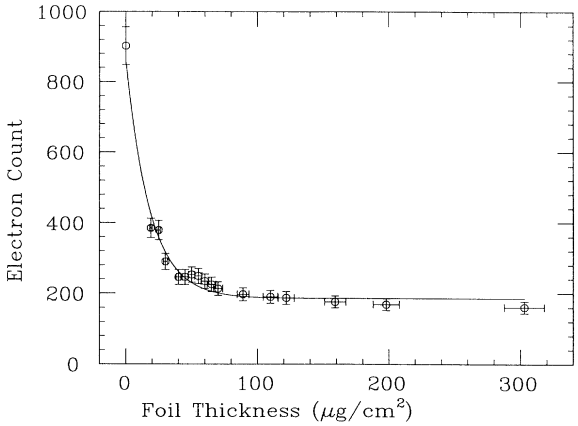

FIG. 12. Relative yield of H^- at 800 MeV as a function of carbon-foil thickness. The solid line in each graph is the best fit to (26).

H^- beam and the constant background. Here x is the foil thickness in μg/cm^2. The results of the best fit to the data are

$$A=675.0\pm53.0\ ,$$

$$b=0.055\pm0.005\ ,$$

$$C=186.0\pm7.0\ ,$$

with a reduced χ^2 of 1.04 giving a confidence level of 41.32%.

3. *Distribution of Rydberg states at 800 MeV*

A Monte Carlo program was developed to propagate a given population distribution of states down the beam line, and to model the field ionization of the surviving states by the electron spectrometer (see Appendix A). The initial n distribution is assumed to be governed by a power law,

$$P(n)=\frac{1}{n^p}\ , \tag{25}$$

and the l substates are assumed to be distributed with a Poisson distribution,

$$P(l)=\exp(-l_c)l_c^l/l!\ , \tag{26}$$

where l_c is the center of the Poisson distribution. The m substates are assumed to be equally distributed. A spectrum is formed by following 10^6 atoms, where the state of each atom is determined from the given distributions, through the beamline and the spectrometer for different values of the spectrometer fields. Each atom is assigned a normally distributed value for its position, momentum, and angular direction. The beam spot is assumed to be 3.0 mm in diameter. The momentum spread and divergence of the beam are taken to be 5.0×10^{-4} and 0.5 mr, respectively. Each Monte Carlo program, a spectrum with 130 points, takes about two hours of CPU time on a VAX/8700 to complete. Hence, due to limitations on

TABLE IV. The results of the best fits of the laserless Monte Carlo spectra to the experimental results taken at 800 MeV.

Foil ($\mu g/cm^2$)	Run number	p	l_c	χ^2/f	CL (%)
19	344	8.0	3.0	0.83	87.0
25	346	8.0	5.0	0.86	82.0
30	347	8.0	5.0	2.27	0.0
35	348	8.0	5.0	3.12	0.0
40	349	7.0	7.0	3.17	0.0
45	350	7.0	7.0	2.93	0.0
50	351	7.0	7.0	2.78	0.0
55	352	7.0	7.0	2.84	0.0
60	353	7.0	7.0	2.84	0.0
65	354	7.0	7.0	3.24	0.0
70	355	7.0	7.0	3.79	0.0
89	356	7.0	7.0	2.84	0.0
110	357	8.0	5.0	2.22	0.0
122	360	8.0	5.0	1.77	0.0
159	359	8.0	5.0	1.49	0.2
198	358	8.0	5.0	1.56	0.1
303	361	8.0	7.0	1.09	26.0

computer time, only 64 Monte Carlo spectra for values of $p=2,3,\ldots,9$ and $l_c=0,1,\ldots,7$ are completed. Therefore, a comparison of the experimental data with the Monte Carlo predictions provides a qualitative estimate on the initial distribution of the Rydberg states coming out of a foil.

The Monte Carlo spectra are fit to a given experimental spectrum by varying an overall scaling parameter until the χ^2 of the fit is minimized. The magnetic field of the spectrometer is read out by a voltmeter interfaced to the data-acquisition system. The conversion factor, volts to gauss, is determined to be 198.1 ± 0.5 G/V. During a fit the conversion factor is also allowed to vary over its range of uncertainty, which is from 197.6 to 198.6. A number of Monte Carlo runs are also performed for a power-law distribution in l, $1/(l+1)^p$, and a statistical distribution in l. It is found that a Poisson l distribution consistently provides a better fit than a power-law l distribution for all the carbon foils. The statistical l distribution results in the lowest confidence levels as compared with the other two distributions. The results of the best Monte Carlo fit, assuming a Poisson l distribution, for each carbon foil are summarized in Table IV.

The Monte Carlo model is successful, as seen from the reduced χ^2 values for the best fits, in predicting the experimental electron spectra for the thinnest and the thickest foils. Figures 13(a) and 13(b) show the electron spectra for the 19- and 70-$\mu g/cm^2$ carbon foils and their respective best fits to the Monte Carlo results. The poor agreement between the experiment and the computer model for the intermediate thicknesses is indicative of processes, such as Stark mixing of l substates, that are not included in the program. The program also assumes the same l distribution for all the $H^0(n)$ states under consideration. These difficulties emphasize the need for the theoretical input in order to limit the choices on various distributions.

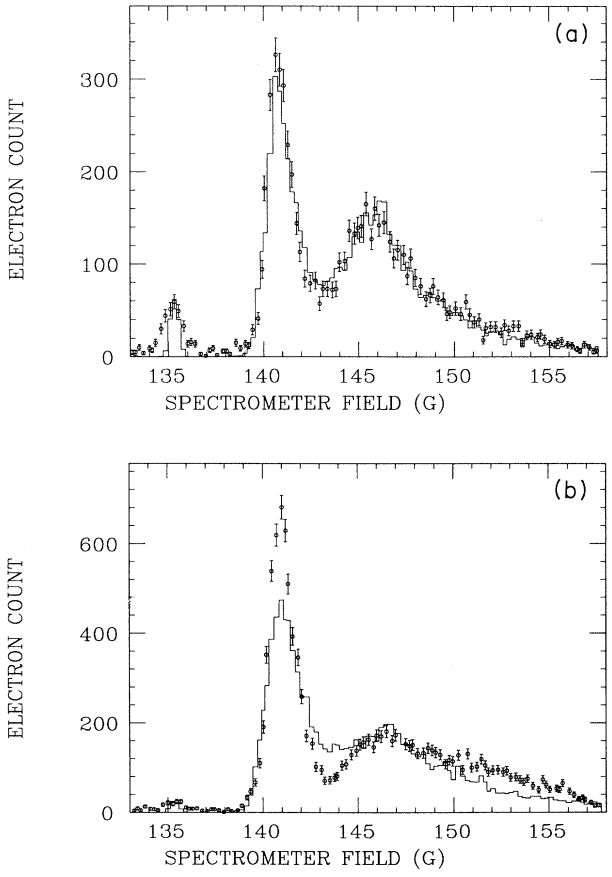

FIG. 13. (a) The best laserless Monte Carlo fit for a 19-$\mu g/cm^2$ carbon foil and (b) the poorest laserless Monte Carlo fit a 70.0-$\mu g/cm^2$ carbon foil at 800 MeV. The histogram in each figure is the best Monte Carlo fit to the data.

TABLE V. Experimental dates and conditions for various laser measurements.

BE (MeV)	Date	State	Macropulse (μs)	Micropulse (ns)
500	July '88	3,4	700	5
581	August '88	2,3,4	800	100
226	October '88	2,3	350	4000
800	July '89	1,2	0.5	5
716	August '89	2	0.5	5
800	August '89	2,3,4,5	400	360

B. Laser data

The details of yield data for low-lying states, taken with the laser method, are discussed. A summary of the experimental conditions is given in Table V.

1. Yield of $n=3,4$ at 500 MeV

These data are taken with the first beam delivered to HIRAB in July of 1988. The polarized H^- beam was directed to HIRAB at a repetition rate of 40 Hz with a macropulse duration of 700 μs, and a microstructure consisting of 1-ns micropulses separated by 5 ns. This experiment, which we regard as preliminary, was hampered by a poor vacuum. However, we were able to observe the $n=3,4$ to $n=12$ transitions.

The laser used was the fundamental wavelength (1064 nm) of a Quanta Ray DCR-2 Nd:YAG laser run in the quasi-cw mode. This provided a laser pulse lasting about 100 μs with 0.6 J per pulse. This mode of running simplified the data taking as the probability of producing multiple signal counts per micropulse was found to be negligible. This fact combined with the low dead time of the detector (20 ns) made it feasible to simply count the interaction products without any loss of accuracy due to multiple hits.

The photon energy in the rest frame of the atoms was fixed at an energy corresponding to the peak of a given transition. A scalar counted the number of electrons detected in coincidence with the laser pulse. A background gate of equal duration to the laser pulse was enabled in the absence of the laser pulse. This measured the rate of the background events. The signal rate was then simply determined by

$$\mathcal{S}=\mathcal{C}_{\rm on}-\mathcal{C}_{\rm off}\ , \tag{27}$$

where $\mathcal{S}$ represents the signal rate, $\mathcal{C}_{\rm on}$ represents counts with the laser on while $\mathcal{C}_{\rm off}$ represents counts with the laser off. The signal for each foil was measured to determine the relative yields of $n=3$ and 4 as a function of foil thickness, which are shown in Figs. 14(a) and 14(b). The solid line in each graph is the best fit to the simple rate equation. The results of the fit are summarized in Table III. Due to lack of laser-power information at various angles, the yields of $n=3$ and 4 are not normalized to each other.

2. Yield of $n=2,3,4$ at 581 MeV

The yields of $n=2,3,4$ as a function of carbon-foil thickness were measured by photoexciting the low-lying states to $n=12$ which was field ionized and the electron detected by the electron spectrometer. The laser pulse as monitored by a fast vacuum photodiode was used to open a 40-ns data gate in coincidence with the laser-produced electrons. The logic gate was used to trigger a CAMAC Analog-to-Digital Converter (ADC) to integrate and digi-

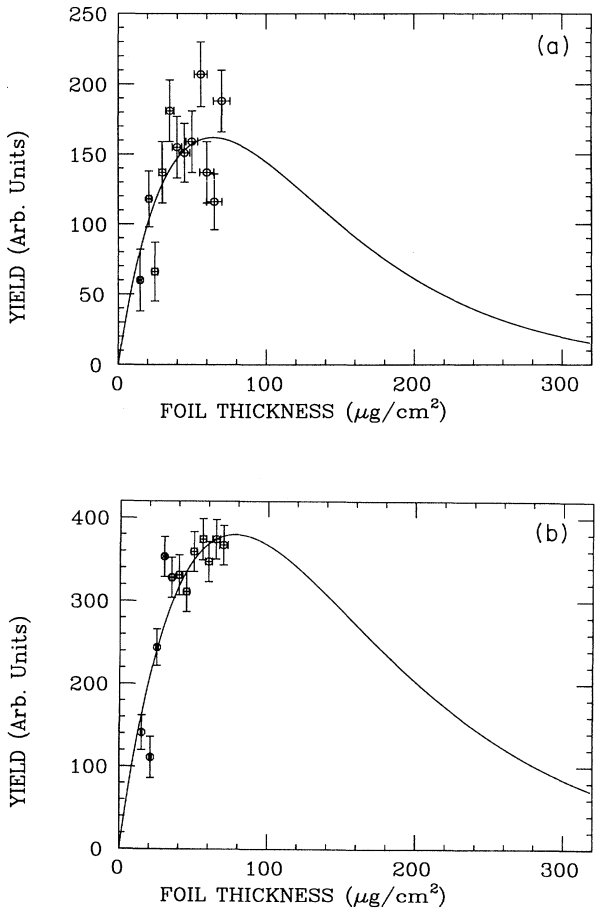

FIG. 14. Relative yield of (a) $n=3$ and (b) $n=4$ at 500 MeV as a function of carbon-foil thickness. The solid line in each graph is the best fit to (5).

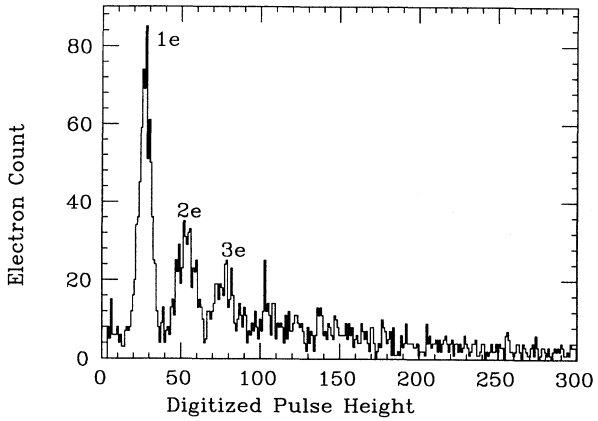

FIG. 15. Example of the electron pulse-height spectrum taken at 581 MeV.

tize the electron pulse. A background gate of equal duration to the laser gate was opened 100 ns later in the beam pulse to estimate the background produced by H^- ions interacting with the residual gas in the beam line. This technique produced an excellent signal-to-background ratio of typically about 100. However, some systematic problems, such as timing drifts and fluctuations in the particle beam intensity, had to be constantly monitored. The high intensity of the laser pulse produced multiple electron counts within a given laser gate. In order to extract the number of electrons detached per laser pulse, an electron pulse-height histogram was formed. Figure 15 provides an example of the pulse-height spectrum, where the horizontal axis is the digitized pulse height and the vertical axis is counts per bin. The peaks in the histogram correspond to an integer multiple of electron hits. The height of each peak is proportional to the probability for the production of a multiple hit. The width of the single-hit peak determines the energy resolution of the plastic scintillator used to detect the electrons. The width of each peak increases with the multiplicity of the hit as the pulse height uncertainties of individual electrons are combined. This effectively smears the higher peaks together. The identity of the lower peaks caused by 1,2,3,... electron hits is easily determined for runs with a low count rate as the lower counts become more probable.

The positions of each peak are found by fitting them to a Gaussian function using an on-line fitting routine. The positions of these peaks are then fit to a straight line given by

$$PH(n)=mn+b \ , \tag{28}$$

where n is the peak number, $PH(n)$ is the pulse height corresponding to the center of each peak, m is the line's slope, and b is the pedestal count for the detection system. Once the slope and pedestal are determined, then the number of electrons detected is given by

$$n=\mathcal{N}\left[\frac{1}{m}(PH-b)\right] \ , \tag{29}$$

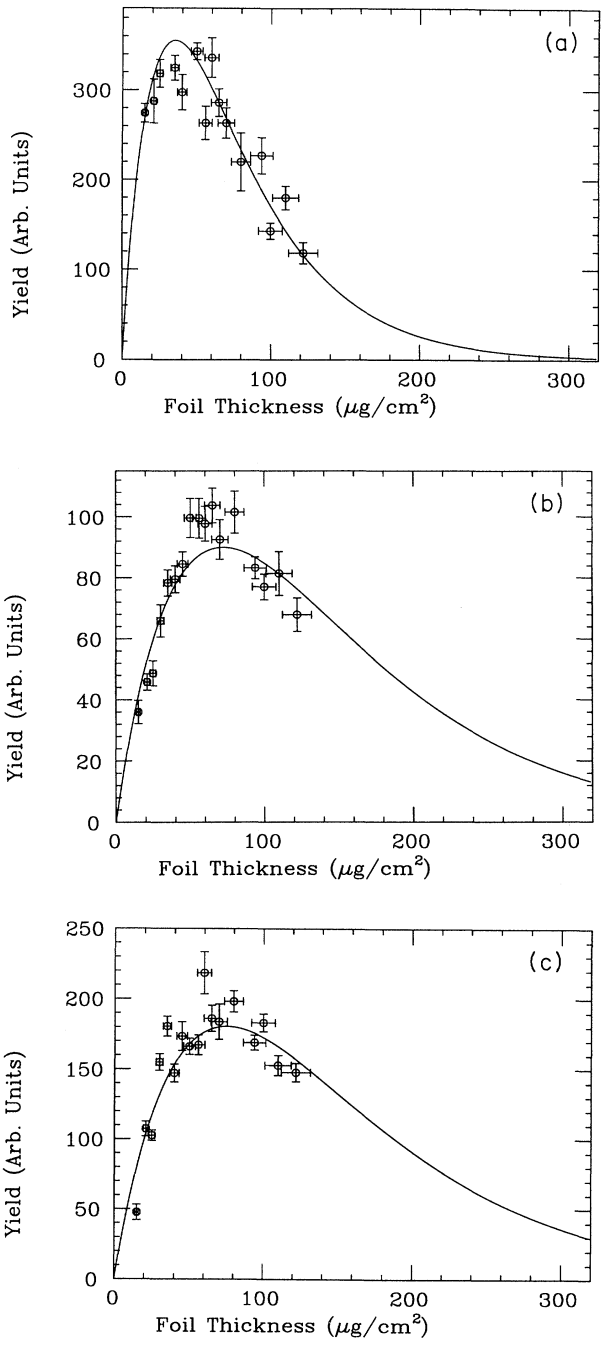

FIG. 16. Relative yield of (a) $n=2$, (b) $n=3$, and (c) $n=4$ at 581 MeV as a function of carbon-foil thickness. The solid line in each graph is the best fit to (5).

where $\mathcal{N}$ represents the nearest integer function. The spectral profile of a transition is constructed by plotting the number of detected electrons versus photon energy and is fit to an asymmetric Gaussian with a constant background. The area under the fitted curve is used as a measure of the yield. This procedure is repeated to obtain data for $n=2,3,4$ transitions to $n=12$ for 17 different carbon foils. Figures 16(a), 16(b), and 16(c) show

the relative yields of the measured low-lying states as a function of foil thickness. The yields of different states are not normalized to each other. The solid curves are again the best fits to the simple rate equation; see Table III for the results.

3. *Yield of n = 2 at 226 MeV*

A 226-MeV H^- beam was delivered in macropulses of about 350 μs wide at a repetition rate of 12 Hz. The microstructure consisted of 1-ns-wide micropulses separated by 4 μs. The Nd:YAG laser beam, passing through a harmonic generator crystal, produced the second harmonic with a photon energy of 2.32 eV at 12 Hz with a laser energy of 30 mJ per pulse. The laser beam was expanded by a factor of 5 to reduce its divergence, resulting in a beam of 2-cm diameter in the interaction region. Apart from these differences, every other aspect of the experiment remained similar to the earlier experiment performed at 581 MeV.

The relative yield of $n=2$ states were measured by Doppler tuning the laser photon energy to excite a transition to $n=15$ which were detected by the electron spectrometer. The spectral lines were fit to an asymmetric Gaussian and the area of the fitted curve was used as a measure of the yield. The details of the analysis remained similar to that of the 581-MeV data. The relative yield of $n=2$ versus carbon-foil thickness is shown in Figure 17. Some of the data points were measured a second time to verify the structure seen in the yield curve. The yield data are fit to the simple rate formula (solid line in Fig. 17), and the results of the fit are found in Table III.

4. *Yield of n = 2 at 716 MeV*

The H^- beam was delivered to HIRAB at 10 Hz. The macropulses lasted for 500 ns with a 5-ns spacing between the micropulses. The fourth harmonic of a Nd:YAG laser was timed to randomly overlap with one or two micropulses. This mode of running solved the problem of long-term drifts in timing which had to be constantly monitored for the case of a microstructure with more than 5-ns spacing between the micropulses. The laser pulse energy was about 50 mJ per pulse.

The relative yield of $n=2$ was measured for all the carbon foils by laser excitation to $n=12$ state and were subsequently field ionized by the electron spectrometer. The data analysis is similar to that of the 581-MeV data. The yield of $n=2$ for various carbon-foil thicknesses is shown in Fig. 18. The data is fit to the simple rate equation, and the results of the fit are summarized in Table III.

5. *Yield of n = 1,2 at 800 MeV*

The structure of the H^- beam was changed for this experiment, producing 500-ns macropulses with a spacing of 5 ns between the micropulses. The 5-ns microstructure eliminated the need to time the laser pulse to coincide with a single micropulse. This avoided the problem of the laser trigger timing drift which had plagued an earlier experiment. In this case, the laser pulse randomly overlapped one or two micropulses. The fourth harmonic of the Nd:YAG laser, with a photon burst of about 8 ns, was used to excite transitions from $n=1,2$ to $n=11$ state. The spectral profiles of these lines were again fit to a Gaussian to get the yield for each state as a function of foil thickness, as shown in Fig. 19(a). The solid line in the graph is the best fit to the simple rate equation. The fitted parameters are tabulated in Table III. The $n=2$ yield measurement [Fig. 19(b)] was plagued by poor statistics; this was repeated in a later run.

6. *Yield of n = 2–5 at 800 MeV*

The fundamental frequency of the Nd:YAG laser used for this run enabled us to probe the populations of $n=2-5$ states. The laser was operated in its non-Q-switched mode with pulses lasting for about 100 μs. The macropulses were 360 μs long with a spacing of 360 ns between the micropulses.

The signal counts in coincidence with the laser pulse were counted using a scalar. This assumed that the probabilities for multiple counts were negligible, as supported

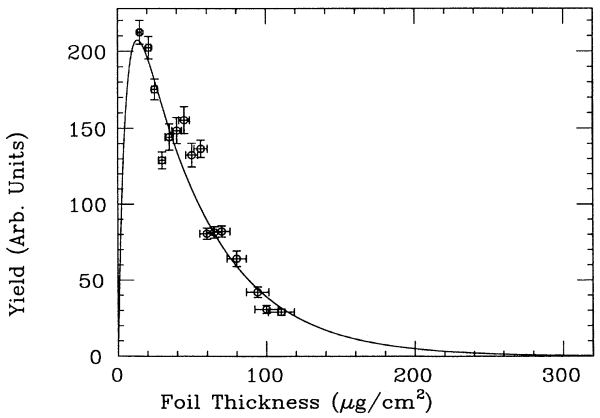

FIG. 17. Relative yield of $n=2$ at 226 MeV as a function of carbon-foil thickness. The solid line is the best fit to (5).

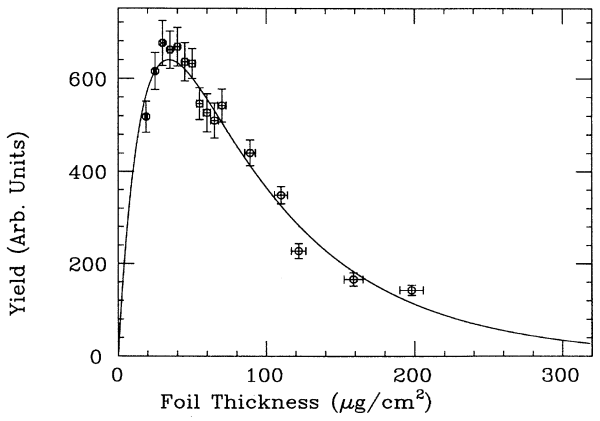

FIG. 18. Relative yield of $n=2$ at 716 MeV as a function of carbon-foil thickness. The solid line is the best fit to (5).

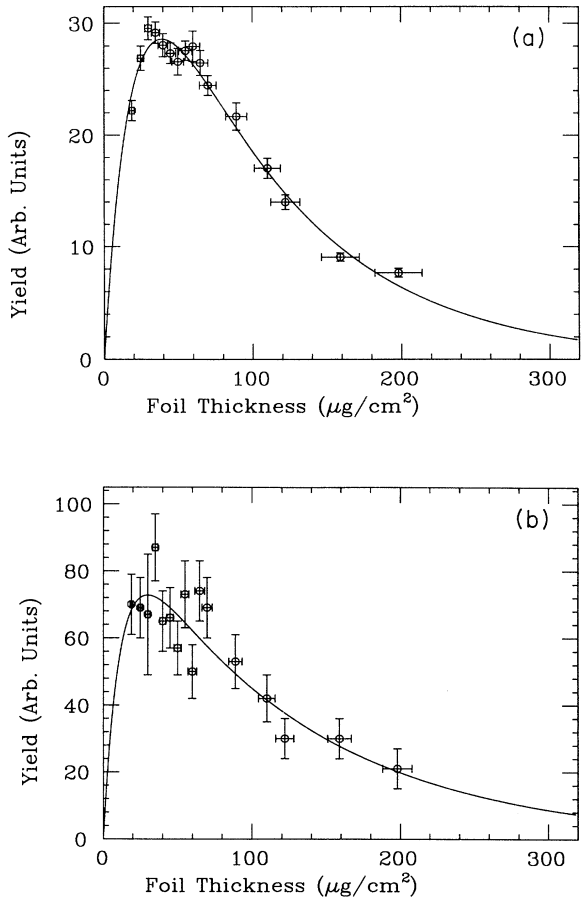

FIG. 19. Relative yield of (a) $n=1$ and (b) $n=2$ at 800 MeV as a function of carbon-foil thickness. The solid in each graph is the best fit to (5).

by a singles rate of 37 per second calculated from Eq. (22). Nevertheless, the pulse height spectrum of the signal electrons showed a significant two electron peak. The pulse-height distribution does not follow a Poisson distribution, as had been expected for this experiment. This is attributed to the coincidence of the spikes in the laser output with micropulses which could well produce two signal counts per micropulse. The pulse-height spectrum at each angle is used to correct the scalar counts for multiple counts. The modified spectral lines are fit to a Gaussian to measure the relative yield of each state. The resulting yield curves are shown in Figs. 20(a)–20(d). The solid line in each graph is the best fit to the simple rate equation. The results of the fit are summarized in Table III.

7. *Distribution of $n=2-5$ at 800 MeV*

A computer simulation is developed to follow a given population distribution of the states of the hydrogen atoms coming out of a foil (see Appendix B for details). The n distribution is again determined by a power law n^{-p} as discussed in Sec. IV A 3. The l substates are assumed to be statistically populated. The Monte Carlo results are normalized to the experimental data at one point and the χ^2 of the fit is computed. A fitting program MINUIT is used to vary the initial n distribution by adjusting the exponent of the power law p until the χ^2 of the fit is minimized. Figure 21 shows the relative yields of the $n=2-5$ for a 45-$\mu g/cm^2$ carbon foil and the normalized yields as predicted by the computer simulation. The results of the fits are summarized in Table VI. Figure 22 illustrates the effect of foil thickness on the exponent of the power law p. The power p is found to decrease with thickness, which means that the excited states become more evenly populated for the thicker foils. This is evidence for a beam-foil interaction mechanism which is, at least, partially diffusive in nature.

V. RESULTS AND CONCLUSIONS

A. Optimized foil thicknesses

In this section the values of the optimized carbon-foil thicknesses, maximizing the yield of a given state, at various beam energies are summarized. The optimum thickness for each case is calculated by applying Eq. (28) to the fitted parameters of the simple rate equation (see Table VII). The value of the full width at half maximum (FWHM) for each yield curve is also reported. The optimum thickness for the production of a particular state n is found to increase with n. Our most complete set of data, illustrated in Fig. 23(a), shows that the maximum production of $n=1$ and $n=2$ states occurs for essentially the same thickness, while it makes a jump, by almost a factor of 2, for $n=3$. The optimum production of $n=4$ continues to be higher than that of $n=3$, and remains unchanged, within error bars, for higher excited states. At the same time, following the same trend, the yield curves become broadened for higher excited states. The

TABLE VI. The results of the best fits of the laser computer simulation to the experimental yields. The fit errors on the exponents are about 0.05.

Foil ($\mu g/cm^2$)	p	χ^2/f	CL (%)
19	3.54	1.55	21.32
25	3.41	0.98	37.47
30	3.02	0.02	98.36
35	3.06	0.04	95.62
40	3.06	0.20	82.27
45	3.26	0.27	76.03
50	2.96	0.02	97.68
55	2.99	0.05	95.02
60	2.76	0.01	99.54
65	2.32	0.45	63.90
70	1.85	2.07	14.98
89	1.98	0.65	52.25
110	1.71	1.13	32.37
122	1.85	1.29	27.48
159	1.29	2.47	8.47
198	1.29	1.38	25.08

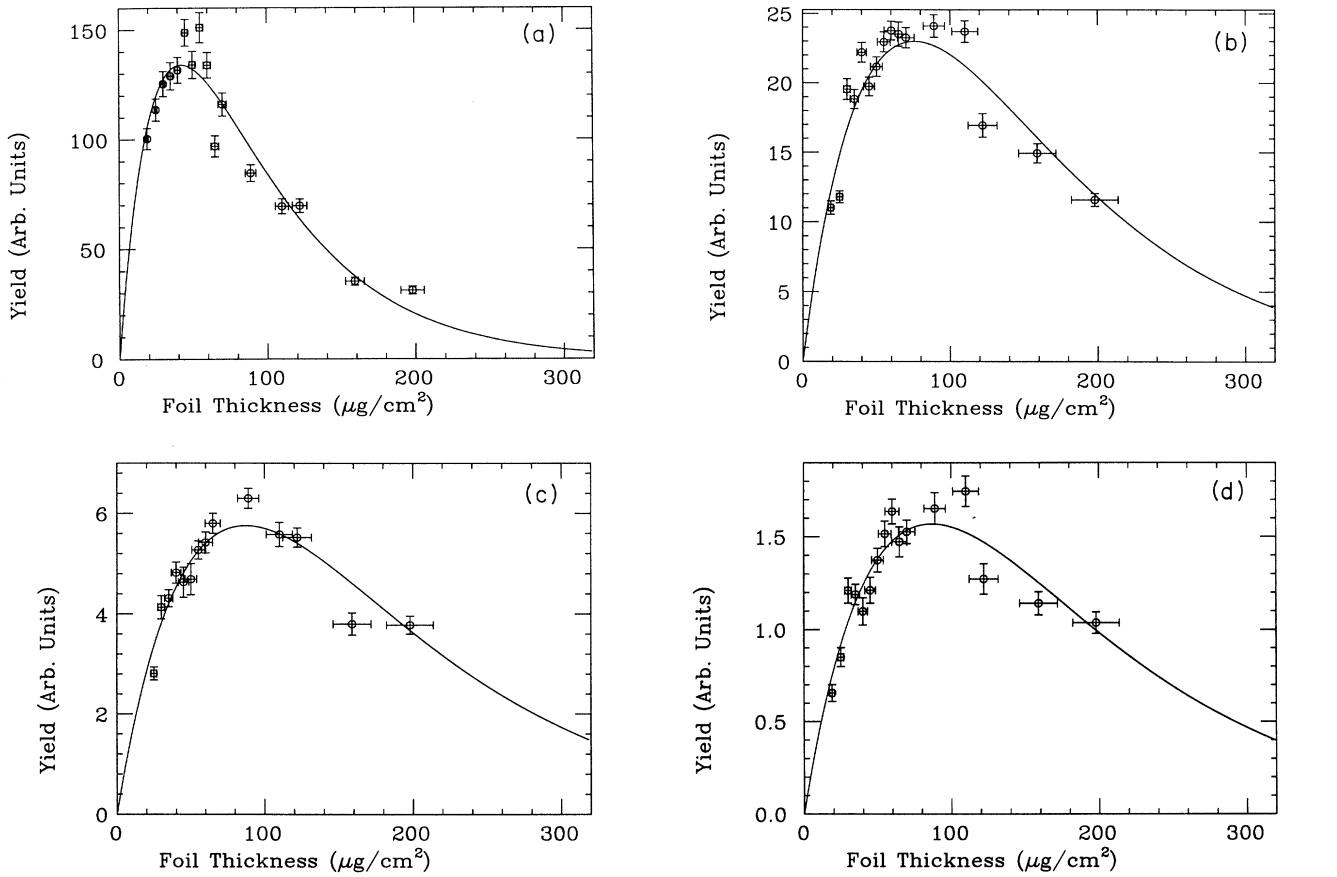

FIG. 20. Relative yield of (a) $n=2$, (b) $n=3$, (c) $n=4$, and (d) $n=5$ at 800 MeV as a function of carbon-foil thickness. The solid line in each graph is the best fit to (5).

fact that $n=1$ and $n=2$ yields peak for the same thickness is specially interesting. This implies that the production mechanisms for these two states may be similar. Once a hydrogen atom in $n=2$ state is produced, then $n=3$ states may be formed from $n=2$ states by subsequent collisions with the target atoms, thus explaining the larger optimum thickness for the $n=3$ yield. In the same fashion, higher excited states may be formed from lower states. However, the binding energies of the highly excited states get closer to each other, which may explain

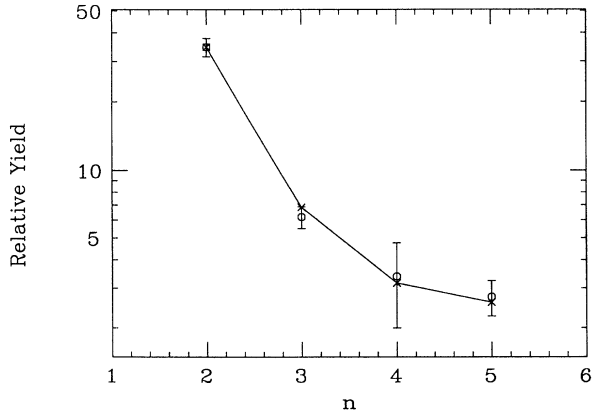

FIG. 21. The best fit of the laser experiment's simulation (crosses) to the 45.0-μg/cm^2 carbon-foil data (circles with error bars).

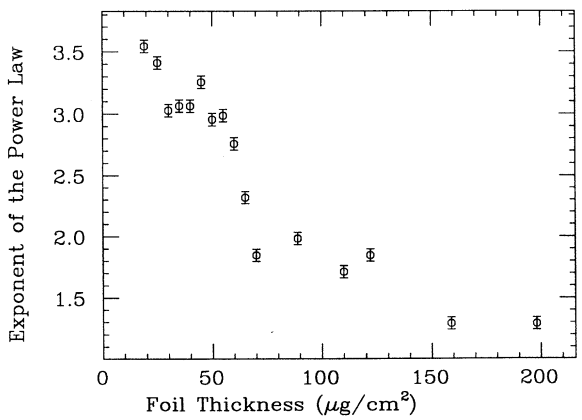

FIG. 22. Exponent of the power law n^{-p} vs carbon-foil thickness at 800 MeV.

TABLE VII. The optimum thicknesses and full width at half maximum (FWHM) of the yield curves for various states and beam energies.

n	BE (MeV)	x_{max} ($\mu g/cm^2$)	FWHM ($\mu g/cm^2$)
1	800	39.8±0.7	117.2
2	800	39.9±0.7	111.1
3	800	76.3±4.4	186.6
4	800	87.7±1.9	214.5
5	800	87.7±2.4	214.6
10	800	90.4±1.3	248.6
11	800	87.7±1.2	217.4
2	716	34.5±1.3	104.5
2	581	35.9±1.1	89.9
3	581	72.3±8.3	176.8
4	581	76.6±4.1	187.3
14	581	91.8±1.1	224.5
3	500	65.4±9.3	160.1
4	500	86.1±4.7	211.0
2	226	17.7±1.5	53.3

why the optimum thickness becomes essentially constant for these states. The same trend persists at 581 MeV, illustrated in Fig. 23(b), and 500 MeV. It is interesting to note that the diameter of $n=1$ state (1.0 Å) is smaller than the lattice spacing (2.0 Å), and the $n=2$ atomic size (4.0 Å) is still on the order of the lattice spacing. However, the diameters of excited states with $n \geq 3$ become much larger than the average distance between the carbon atoms in a foil, providing a clue as to why the production mechanisms for these states might be different from that of $n=1$ and $n=2$.

The effect of the beam energy on the optimum thickness for production of $n=2$ state is illustrated in Fig. 24(a). The optimum thickness is expected to increase with energy as the ion spends less time inside a foil. Another equivalent approach to this problem is to notice that the thickness of a foil is Lorentz contracted by a factor of γ. Figure 24(b) shows the modified optimum thickness (X_{max}/γ) as a function of beam energy. The corrected data points are fit to a horizontal line which gives

$$X_{max}=20.6\pm0.5\ \mu g/cm^2\ ,$$

$$\chi^2/f=10.9\ ,$$

with a confidence level of 1.2%, indicating that Lorentz

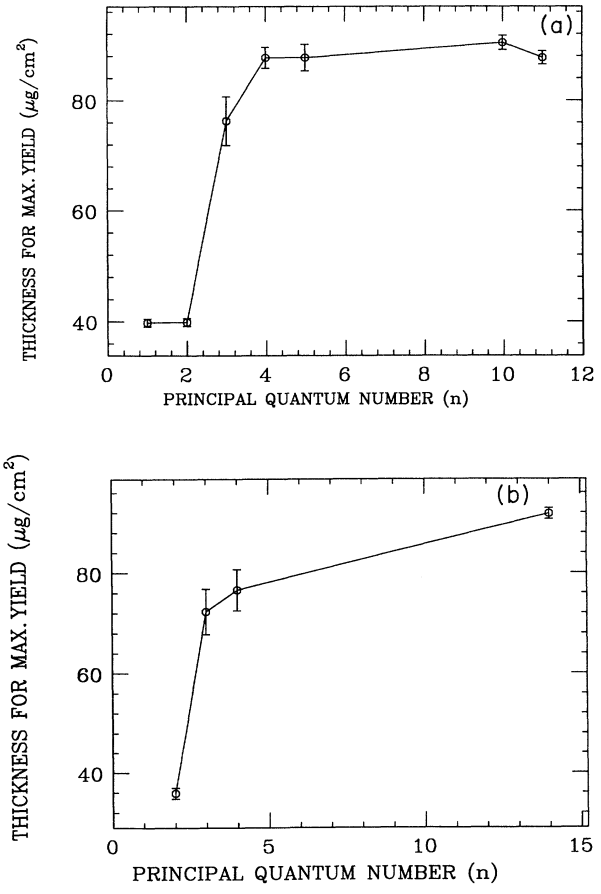

FIG. 23. Optimum thickness versus n at (a) 800 and (b) 581 MeV.

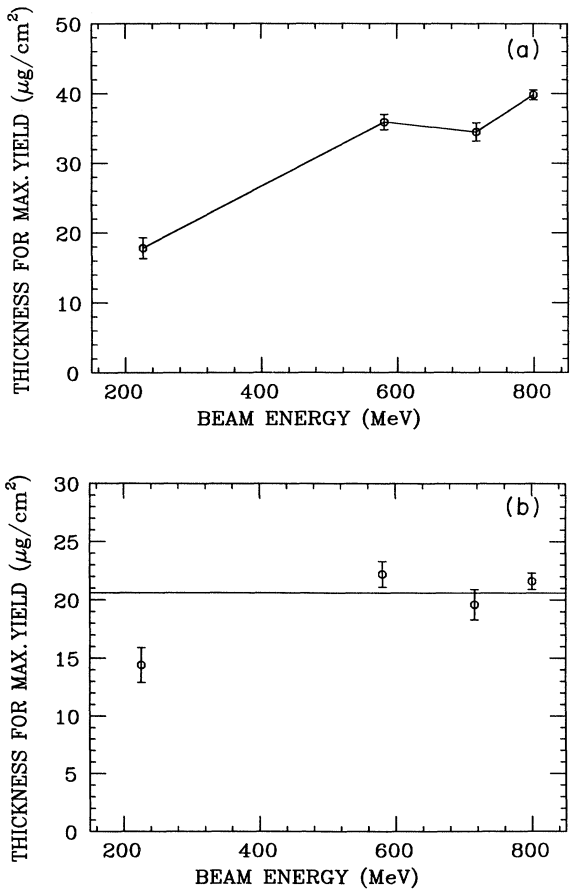

FIG. 24. (a) Optimum thickness for $n=2$ and (b) modified optimum thickness, divided by γ, for $n=2$ vs beam energy.

contraction is not successful in explaining the increase in optimum thickness with beam energy. The significant deviation of optimum thickness at 226 MeV from a straight line is suggestive of new processes taking effect at low energies.

The optimum thicknesses for production of $n=3$ at 800, 581, and 500 MeV are also normalized to γ for each energy, giving 41.2, 44.6, and 42.7 μg/cm^2, respectively. The modified data are fit to a horizontal line, giving

$$X_{\max}=42.3\pm1.7\ ,$$

$$\chi^2/f=0.48\ ,$$

with a confidence level of 78.7%, in agreement with the Lorentz contraction hypothesis.

B. Distribution of states

A number of Monte Carlo programs are used to estimate the distribution of the states leaving a foil at 800 MeV. The n distribution is assumed to be governed by a power law n^{-p} which is the finding of some low-energy (beam energy less than 1.0 MeV) studies.[7–9] It is found that the exponent of the power law p for a given foil is larger for Rydberg states than the exponent for the low-lying states. For example, for a 25.0 μg/cm^2 carbon foil, it is found that $p=8.0\pm1.0$ for the production of Rydberg states ($n=10,\ldots,14$), and $p=3.41\pm0.05$ for the low-lying states ($n=2,\ldots,5$). This is indicating that a single power law is unable to characterize the n distribution of excited states over a wide range of n. This demonstrates the need for theoretical guidance for a new functional form, possibly an exponential n distribution ($e^{-\alpha n}$), where the distribution is changed with n. The possibility of an exponential n distribution points to a diffusive process.

A computer simulation of the laser experiment shows that the n distribution of the low-lying states at 800 MeV is modified by changing the foil thickness. In particular, the distribution changes from $n^{-3.54}$ for a 19.0-μg/cm^2 carbon foil to $n^{-1.29}$ for a 198.0-μg/cm^2 foil, which indicates that the states become more evenly populated for the thicker foils.

The laserless Monte Carlo simulation finds that the n distribution of the Rydberg states is not affected much by changing the foil thickness. However, the l distribution of the substates is found to include consistently a proportionally large number of high-angular-momentum states for all the foils. As an example, the peak of the assumed Poisson l distribution for a 35.0-μg/cm^2 carbon foils occurs at $l=5.0$, implying that there are more f substates than s and p substates. This is a deviation from the low-energy theories, where the excited states are thought to be formed at the exit surface of a foil. Here the single ion-atom conditions favor the low-l substates. This is further evidence for a stochastic diffusive process in a foil where a proportionally large number of high-l states may be formed.

C. Outcome of the foil studies

The relativistic H^--foil experiments have been successful in opening the doors to previously unexplored territory. For the low-energy experiments, the surface of a foil plays an important role in the formation of the excited state emerging from the foil. However, for the case of the high-energy interaction of H^- ions with foils, the yield of a given state is observed to be strongly dependent on the foil thickness. This demonstrates that the bulk effects dominate surface effects, if any, during the beam-foil interaction. This is not surprising, considering that the high energy of the projectile particles does not allow for electron capture from the target atoms. The excitation occurs while the H^- ions are traversing through the foil. It is also interesting to note that the orbiting electrons of the projectile barely move during their passage through a foil. This means that the state of the projectile must be decided sometime after it leaves a foil, in order for the electrons to reach their classical orbits.

The observed yields for a given state as a function of foil thickness are fit to the simple rate equation (see Sec. II A). For most cases the fits result in a reduced χ^2 considerably greater than 1.0, indicating a poor agreement between the experimental data and the simple model. The simple model is truly oversimplifying the interaction process. Some of the observed structures in the yield curves, e.g., the $n=2$ yield at 226 MeV, are also indicative of more complex processes, such as a coherent excitation of the H^- ion, where a group of target atoms may interact simultaneously with the passing ion.

The optimum carbon-foil thickness for the production of a given state at 800 MeV is found to vary with the principal quantum number n of a state. In particular, the yields of $n=1$ and $n=2$ states peak roughly at the same thickness (about 40 μg/cm^2), indicating that the processes for the production these states are similar. A sudden jump in the optimum thickness at $n=3$ is observed. The trend continues for $n=4$, but it then levels off for the higher states. The $n=3$ state marks the transition in atomic size where it is larger than the lattice spacing of the carbon atoms. The yield curves for states with $n>2$ also become wider than the ones for $n=1,2$. This is all evidence that a new mechanism is taking over the production of $n=3$ and higher states which is at least partially diffusive. The same trend persists at 581 and 500 MeV.

A number of Monte Carlo programs are used to estimate the distribution of the states leaving a foil. The Rydberg states are found to contain a higher proportion of high-l states than low-l states. The distribution of the low-lying states is significantly modified by changing the foil thickness, such that the states become more evenly populated for the thicker foils.

Even though these experiments have been successful, to some extent, in illuminating the problem of a relativistic H^- ion interacting with a thin foil, a comprehensive theoretical study is needed to clearly interpret the experimental results.

ACKNOWLEDGMENTS

The authors would like to acknowledge technical support from Lawrence Quintana, Fred Montoya, Art Gonzales, and Fred Roybal at Los Alamos, and from Jim Hontas, Jesus Sanchez, and Bill Miller at the University of New Mexico. We are grateful for the assistance of many others, including Joey Donahue, Jim Knudson, Tom Altman, and Dan Rislove. This work was supported by the division of Chemical Sciences, Office of Basic Energy Sciences, Office of Energy Research, U.S. Department of Energy, and was also funded in part by the U.S. Army Strategic Defense Command.

APPENDIX A: A MONTE CARLO SIMULATION OF THE LASERLESS EXPERIMENT

A Monte Carlo program[29] was developed to follow a given distribution of excited states of hydrogen down the beam line to the position of the electron spectrometer. The field ionization of the remaining atoms as they enter the electron spectrometer is modeled. The trajectories of liberated electrons are followed to check if they hit the detector. A spectrum is formed by plotting the number of "hits" versus the spectrometer field. The momentum spread of the beam, the divergence, and the beam spot size are all built into the program assuming a Gaussian spread in all of the above parameters. A momentum spread of 5×10^{-4}, a beam divergence of 0.5 mrad, and a beam spot size of 3.0 mm are assumed. The program is successful in replicating the general features of the experiment.

The first step is to calculate the initial distribution of $H^0(n,l,m)$ as determined by a number of parameters set by the user. The n distribution is determined by a power law as given by

$$\mathcal{P}(n)=\frac{K_n}{n^{pn}} , \tag{A1}$$

where pn is input into the program, $\mathcal{P}$ is the population function, and K_n is determined from

$$K_n=N\Big/\sum_n \frac{1}{n^{pn}} , \tag{A2}$$

where N is the total number of atoms to be followed. This functional form is based on predictions at low energies. A second functional form

$$\mathcal{P}(n)=K_n e^{-\alpha n} , \tag{A3}$$

is also used to determine n distribution of the hydrogenic states. However, there are no functional forms available for the l distribution within an n manifold. For a lack of a better model, two functional forms are used. The first is an extension of the model used to calculate the n distribution, which is given by

$$\mathcal{P}(n,l)=\frac{K_{nl}}{(l+1)^{pl}} , \tag{A4}$$

where again pl is an input into the program. The second is the Poisson distribution function, which is

$$\mathcal{P}(n,l)=K_{nl}e^{-pl}\frac{(pl)^l}{l!} , \tag{A5}$$

where pl now determines the center of the distribution which in principle can vary from 0 to ∞. K_{nl} is determined in the same manner as that of K_n. An equal distribution in m is assumed for the present results. However, the program contains a section which can vary the m distribution according to

$$\mathcal{P}(n,l,m)=\frac{K_{nlm}}{(|m|+1)^{pm}} . \tag{A6}$$

An equal population in m is reached by setting $pm=0$.

The next step is to project from the spherical states (n,l,m) to the parabolic states (n_1,n_2,m), where

$$n=n_1+n_2+|m|+1 . \tag{A7}$$

This is to prepare for the upcoming interaction with the motional electric fields produced by the sweep magnet and the electron spectrometer. Each state (n,l,m) is projected to a number of parabolic states (n_1,n_2,m) as allowed by the above relationship. The following formula is used to compute the probability for each possible projection. The $O(4)$ symmetry of the hydrogenic atoms is used to obtain the formula[35]

$$\langle n_1,n_2,m\,|n,l,m\rangle=(-1)^{(2n_2+|m|-m)/2}C[\tfrac{1}{2}(n-1),\tfrac{1}{2}(n-1),l;\tfrac{1}{2}(m+n_2-n_1),\tfrac{1}{2}(m+n_1-n_2),m'] , \tag{A8}$$

where, in the notation of Rose, $C(j_1,j_2,j;m_1,m_2,m)$ is the angular-momentum Clebsh-Gordon coefficient.

Now, we are ready to face the sweep magnet, which is a dipole magnet. The magnetic field in each bin is assumed to be constant. The falling part of the field is not included in the program since, if a state survives the maximum field in the magnet, it also survives the decreasing field. This assumption is verified by running this section of the program with and without the decreasing section. The magnetic field is transformed to crossed magnetic and electric fields in the rest frame of the atom, given by

$$B=\gamma B , \tag{A9}$$

$$F=\gamma v B_\perp , \tag{A10}$$

where γ and β are the usual relativistic parameters, and v is the atom's velocity, which in this case is perpendicular to the direction of the magnetic field. The strength of the motional electric field for a given bin in the magnet is determined by Eq. (A13). The lifetime of each parabolic state for a given electric field is determined using the uncertainty relationship

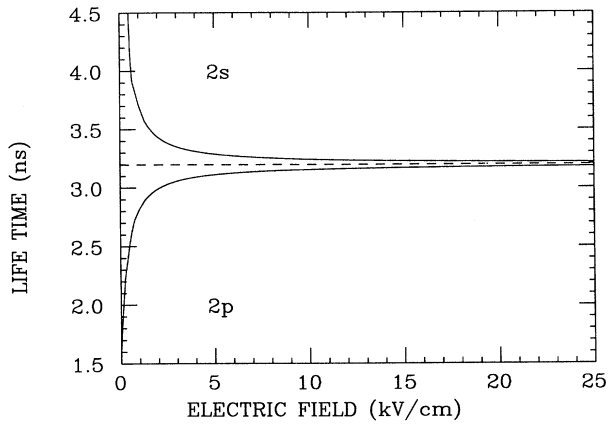

FIG. 25. The effect of an external electric field on the lifetimes of the $2s$ and $2p$ states.

$$\tau\Gamma=\hbar\ , \tag{A11}$$

where Γ is the energy width of the given state. A semiempirical formula for Γ is derived by Damburg and Kolosov:[36]

$$\Gamma=\frac{(4R)^{2n_2+m+1}}{n^3 n_2!(n_2+m)!}$$

$$\times\exp\left[-\tfrac{2}{3}R-\frac{n^3F}{4}(34n_2^2+34n_2m+46n_2+7m^2+23m+\tfrac{53}{3})\right]\ , \tag{A12}$$

where F is the electric field in atomic units, and R is a parameter given by

$$R=(-2E)^{3/2}F^{-1}\ , \tag{A13}$$

where E is the Stark energy of the state. Damberg and Kolosov derive an approximate expression to compute the Stark energy using the perturbative theory by the method of successive approximations. The formula, accurate up to the fifth order in F, is found in Ref. 36.

Having computed the lifetime of the state in question, the population of the state surviving the electric field of the cell is calculated by

$$N=N_0e^{-t/\tau}\ , \tag{A14}$$

where t is the time the atoms spend in the cell given by

$$t=\frac{x}{\gamma\beta c}\ , \tag{A15}$$

and x is the cell length in the laboratory frame. All the atoms are propagated through the sweep magnet and the surviving states are sent to the electron spectrometer.

The vertical component of the magnetic field of the spectrometer in a horizontal plane containing the beam is mapped with a grid of $0.25''\times0.5''$ A subroutine is used to perform a linear two-dimensional interpolation to calculate the magnetic field at any point within the spectrometer. The program chooses a maximum field for the spectrometer which is multiplied with the normalized mapped field. Each state is then propagated through the spectrometer in small steps where the lifetime is computed using Eq. (A11). The step size is chosen by decreasing it until no significant change in outcome is observed. The equations of motion for the liberated electrons are readily solved by realizing that the speed of the electrons, hence γ, remains constant. Once an atom decays, a Gaussian distributed[37] position and velocity are assigned to the freed electron, taking into account the finite width and the momentum spread of the beam. All the liberated electrons are followed through the spectrometer and checked to see if they hit the detector. Finally, a spectrum is formed by plotting the total number of hits for each magnet field setting of the spectrometer.

APPENDIX B: A SIMULATION OF THE LASER EXPERIMENT

A program[29] was developed to simulate the process of the laser-excitation of the hydrogen atoms produced in a foil. The initial distribution is determined using the method discussed in Appendix A. The atoms travel through a region which is assumed to be free of any fields. The population of each state is modified by

$$\mathcal{P}(n,l)=\mathcal{P}_0(n,l)\exp\left[\frac{-x}{\gamma\beta c\tau}\right]\ , \tag{B1}$$

where x is the length of the free decay region, and τ is the natural lifetime of the state. Next, the atoms go through the sweep magnet which is set to field ionize states with $n>6$. The motional field alters the lifetime of the low-lying states by Stark mixing the l substates. The effect of an external electric field on the lifetimes of $2s$ and $2p$ states[38] is shown in Fig. 25. Assuming that the substates are fully mixed, the lifetimes are simply given by

$$\tau(n,l)=2.0\times\tau(n,1)\ , \tag{B2}$$

where $\tau(n,1)$ is the field-free lifetime of the $\not{\ell}$ states. The population of each state is modified for decays within the magnet and the following field-free region using Eq. (B4). At the end of each of the three regions, from the transition probability for each decayed atom, the populations of the lower states are updated.

The next step is to model the laser excitation of the surviving states $P(n,l)$ to a Rydberg state. The effect of the experimental resolution is to broaden the natural spectral lines which are Lorentzian in shape. One important observation is that areas under the spectral profiles are conserved even as they are convoluted by a Gaussian function representing the experimental resolution. The total rate of photoabsorption (i.e., the area under the spectral line) is given by

$$R_n=K\frac{1+\beta\cos\alpha}{\beta\sin\alpha}\sum_{l=0}^{n-1}\mathcal{P}(n,l)\sigma_l\Delta E\ ,$$

where K is an overall normalization factor, and ΔE is the natural linewidth. The photoabsorption cross section σ_l

is calculated using the following equation:[39]

$$\sigma(\omega_0)=\tfrac{4}{3}\pi^2\alpha_c\omega_0|\langle u|\mathbf{r}|l\rangle|^2\frac{g(\omega_0)}{gl}\ , \tag{B3}$$

for electric dipole absorption far from saturation. In this equation

$$\alpha_c=\frac{1}{137.036}\ , \tag{B4}$$

$$\omega_0=\frac{E(u)-E(l)}{\hbar}\ , \tag{B5}$$

$|\langle u|\mathbf{r}|l\rangle|$ is the dipole-moment matrix element evaluated using the Gordon formula,[40]

$$g_l=2l+1 \tag{B6}$$

is the degeneracy of the lower state, and

$$g(\omega_0)=\frac{1}{\pi\Delta\omega} \tag{B7}$$

is the value at the center of the spectral line profile, assumed to be a Lorentzian with full width at half maximum of $\Delta\omega$.

A fitting program MINUIT is used to fit the theoretical yields to the experimental ones.[34] This is done by changing the initial distribution of the excited states until the χ^2 of the fit is minimized.

*Currently at University of Illinois, Champaign, IL 61820.
†Permanent address: California State University, Long Beach, CA 90840.
‡On leave from the Ferdowsi University, Mashhad, Iran.

[1]T. G. Eck, Phys. Rev. Lett. **33**, 1055 (1974).
[2]Y. Yamazaki *et al.*, Phys. Rev. Lett. **61**, 2913 (1988).
[3]Joachim Burgdorfer and Chris Bottcher, Phys. Rev. Lett. **61**, 2917 (1988).
[4]W. Brandt, in *Atomic Collisions in Solids,* edited by S. Datz, B. Appleton, and C. Moak (Plenum, New York, 1975), p. 761.
[5]D. P. Almeida *et al.*, Phys. Rev. A **36**, 16 (1987).
[6]K. Dybdal *et al.*, Nucl. Instrum. Methods Phys. Res. B **13**, 581 (1986).
[7]June Davidson, Phys. Rev. A **12**, 1350 (1975).
[8]T. Aberg and O. Goscinki, Phys. Rev. A **24**, 801 (1982).
[9]C. J. Anderson *et al.*, Phys. Rev. A **22**, 822 (1980).
[10]N. H. Tolk *et al.*, Nucl. Instrum. Methods **202**, 247 (1982).
[11]J. D. Garcia, Nucl. Instrum. Methods **90**, 295 (1970).
[12]H. C. Bryant *et al.*, Phys. Rev. Lett. **28**, 228 (1977).
[13]P. A. M. Gram *et al.*, Phys. Rev. Lett. **40**, 107 (1978).
[14]M. E. Hamm *et al.*, Phys. Rev. Lett. **43**, 1715 (1979).
[15]J. B. Donahue *et al.*, Phys. Rev. Lett. **48**, 1538 (1982).
[16]S. Cohen *et al.*, Phys. Rev. A **36**, 4728 (1987).
[17]H. C. Bryant *et al.*, Phys. Rev. Lett. **58**, 2412 (1987).
[18]H. C. Bryant, *Atomic Spectra and Collisions in External Fields II* (Bedford New College, London, 1987).
[19]W. W. Smith, in *Atomic Excitation and Recombination in External Fields,* edited by M. H. Nayfeh and C. W. Clark (Gordon and Breach, New York, 1985).
[20]D. W. MacArthur *et al.*, Phys. Rev. Lett. **56**, 282 (1986).
[21]C. Y. Tang, *et al.*, Phys. Rev. A **39**, 6068 (1989).
[22]Donald J. Liska, LANL Report No. LA-4795-MS (1971) (unpublished).
[23]V. A. Bazylev and A. V. Demura, Phys. Lett. **91A**, 369 (1982).
[24]A. J. Jason *et al.*, LANL Report No. LA-UR-81-831 (1981) (unpublished).
[25]T. F. Gallagher, Rep. Prog. Phys. **51**, 154 (1988).
[26]E. J. Galvez *et al.*, Phys. Rev. Lett. **61**, 2011 (1988).
[27]Q. Su *et al.*, Phys. Rev. Lett. **64**, 862 (1990).
[28]M. Font, Phys. Rev. A **40**, 5659 (1990).
[29]A. H. Mohagheghi, Ph.D. thesis, University of New Mexico, 1990.
[30]P. G. Harris, Ph.D. thesis, University of New Mexico, 1990.
[31]J. N. Knudson, LANL Report No. MP-7-TN-23 (1990) (unpublished).
[32]P. G. Harris *et al.*, Nucl. Instrum. Methods A (to be published).
[33]H. C. Bryant *et al.*, Phys. Rev. Lett. **27**, 1928 (1971).
[34]LAMPF Data Analysis Center, MINUIT Under VAX/VMS, Office Memorandum, (1979).
[35]J. W. B. Hughes, Proc. Phys. Soc. London **91**, 810 (1967).
[36]R. J. Damburg and V. V. Kolosov, *Rydberg States of Atoms and Molecules,* edited by R. F. Stebbings (Cambridge University, Cambridge, England, 1983), Ch. 3.
[37]W. H. Press *et al.*, *Numerical Recipes* (Cambridge University, Cambridge, England, 1986).
[38]R. A. Reeder, LANL Technical Note Report No. At-2-BS (1986) (unpublished).
[39]B. H. Bransden and C. J. Joachain, *Physics of Atoms and Molecules* (Longman, New York, 1984).
[40]Hans A. Bethe and Edwin Salpeter, *Quantum Mechanics of One- and Two-Electron Atoms* (Academic, New York, 1957).